

Spin-encoded Wavelength-space Multitasking Janus Metasurfaces

He-Xiu Xu (✉ hxxuellen@gmail.com)

College of Physics and Electronic Engineering, Hengyang Normal University, Hengyang 421002, China
<https://orcid.org/0000-0003-2288-2879>

Chaohui Wang

Air Force Engineering University

Yanzhao Wang

Air Force Engineering University

Mingzhao Wang

Air Force Engineering University

Shaojie Wang

Air Force Engineering University

Guangwei Hu

National University of Singapore

Shiwei Tang

Ningbo University

Yongjun Huang

University of Electronic Science and Technology of China

Xiaohui Ling

Hengyang Normal University

Wei Huang

Northwestern Polytechnical University

Cheng-Wei Qiu

National University of Singapore

Research

Keywords: Chirality, Fano splitting, Janus metasurface, wavelength-space multitasking, spin wave control

Posted Date: December 7th, 2020

DOI: <https://doi.org/10.21203/rs.3.rs-120169/v1>

License:   This work is licensed under a Creative Commons Attribution 4.0 International License.

[Read Full License](#)

Spin-encoded wavelength-space multitasking Janus metasurfaces

By He-Xiu Xu^{1,2,6*}, Chaohui Wang¹, Yanzhao Wang¹, Mingzhao Wang¹, Shaojie Wang¹, Guangwei Hu³, Shiwei Tang⁴, Yongjun Huang⁵, Xiaohui Ling⁶, Wei Huang^{2*}, Cheng-Wei Qiu^{3*}

¹*Air and Missile Defense College, Air Force Engineering University, Xi'an 710051, China*

²*Institute of Flexible Electronics, Northwestern Polytechnical University, Xi'an 710072, China*

³*Department of Electrical and Computer Engineering, National University of Singapore, Singapore 117583, Singapore*

⁴*Department of Physics, Faculty of Science, Ningbo University Ningbo 315211, China*

⁵*School of Information and Communication Engineering, University of Electronic Science and Technology of China, Chengdu 611731, China*

⁶*College of Physics and Electronic Engineering, Hengyang Normal University, Hengyang 421002, China*

*Corresponding Authors: He-Xiu Xu, E-mail: hxxuellen@gmail.com; Wei Huang, E-mail: iamwhuang@nwpu.edu.cn; Cheng-Wei Qiu, E-mail: eleqc@nus.edu.sg

Keywords: Chirality, Fano splitting, Janus metasurface, wavelength-space multitasking, spin wave control

Abstract: The fruitful progress toward light manipulation in reflective (R) or transmissive (T) geometry (half-space) has facilitated strong aspiration to achieving full-space electromagnetic wave control in both R and T channels. Although it promises large-capacity and integrated functionality, yet imposes *prohibitive* difficulty and big challenging for extreme wave control (direction of arrival in full space) via an ultrathin flat device. As of today, very limited demonstrations were reported for single-band and linear-polarization operation, significantly limiting the exploitable degree of freedoms (DoFs) for real-world applications. Herein, we report for the first time a triple-layer wavelength-space multitasking scheme for wide-angle and large-capacity detection. Two anisotropic sub-meta-atoms are engineered with high quality factor and simultaneous in-plane and out-of-plane symmetry breaking, facilitating four R and two T spin-conversion channels with high efficiency and insulation. The chirality-assisted Fano effect gives rise to the wide-angle operation and boosted channels. Above features and released DoF would be extraordinary beneficial for large-capability and angle-engineered advanced device. Two proof-of-concept metadevices, i.e., large-scanning kaleidoscopic-beam generator and a wide-angle large-capacity reverser for multi-target tracking, are devised to verify the significance. Numerical and experimental results have approved predesigned advanced functions at six channels with measured efficiency over 75%. Our findings in multi-DoF multitasking of metasurfaces could stimulate great interest in radar applications with versatile beam generation and multi-channel integration.

1. Introduction

The manipulation of electromagnetic (EM) waves in both reflection (R) and transmission (T), more specifically the full-space direction of arrival (DOA), is highly intriguing for *extreme* scanning and blind-free radar detection since it considerably extends the spatial scope of a system.

One common strategy involves arranging several antenna submodules into a quasi-fan shape to extend their scanning angle^[1], which, however, requires complicated fabrication techniques and suffers from low figure of merits due to the inter-plate interference and spatial polarization disorder. In the past decade, we have witnessed explosive study on metasurfaces for offering on-demand EM wave control in R or T half-space engineering ^{[2]-[8]}. Unfortunately, very limited attempts have been devoted to functional metasurfaces for simultaneous control of radiations^[9] or scatterings ^{[10]-[14]} in the channel of both R and T . This is because T - R grouped strategy via an ultrathin flat device imposes *great* complexity and difficulty in implementation. Nevertheless, all these attempts are confined to single-band and linearly-polarized (LP) operation, and most importantly only two independent degree of freedoms (DoFs), i.e., polarization and propagation direction, are exploited. Interestingly, direction-selected versatile functionalities were realized in two asymmetric T channels of incidence from two sides of an anisotropic metasurface ^[15]. However, it remains unknown how to tailor the R channel and how to extend the functions beyond LP light. Moreover, to enhance the functional capability in full space, more DoFs should be invoked and novel designs should be devised for multitasking metasurfaces. Recently, exploiting the wavelength as a new DoF promises the highly integrated metasurfaces with high stability, reliability and integration ^{[16]-[22]}. But wavelength-encoded full-space operation is challenging in a thin metasurface as it requires to simultaneously control the dispersion, mode decoupling and crosstalk elimination.

Spin is an exclusive polarization state in complementary to its LP counterpart and is extremely crucial for spin optics and EM engineering. Recently, we have witnessed tremendous progresses toward spin wave control, such as spin-decoupled bi-functionalities ^{[23]-[27]}, spin-selective full-dimensional manipulation of optical waves ^[28], spin-induced orbital angular momenta ^{[29],[30]},

photonic spin Hall effect ^{[31],[32]}, and spin-triggered metadevices ^{[33]-[36]}, to name a few. Unfortunately, only the single DoF of *spin* was employed and most have not involved dynamic phase for near unity efficiency. Intuitively, one may wonder to combine above wavelength- and space-multiplexing strategy in LP case for spin-wave modulation. However, this is particularly challenging or inapplicable since the preservation of high efficiency for concentric sub-atoms with spatially varied orientations is *prohibitively* difficult across several wavelengths and in both *R* and *T* channels. In fact, the criteria are typically mutually exclusive for above compound multitasking. A noninterleaved synergetic strategy by involving different propagation dispersion at different wavelengths ^[37] or by merging different momentums ^[38] has significantly enriched the spin-triggered output patterns, however, they were all confined to *T* channel because the basic monolayer meta-atom (nanobrick) without symmetry breaking is inherently far insufficient for direction selectivity. To date, spin-enabled wavelength-multiplexing or space-multiplexing remains elusive and in its infancy in half space, not to mention the compound multitasking of more than above two DoFs in full space.

In light of aforementioned challenges, here we report for the first time a chirality-assisted multitasking strategy by involving simultaneously in-plane and out-of-plane symmetry breaking for extreme spin-wave manipulations across triple wavelengths and along *R&T* channels of two-sided metasurfaces in analog to two faces of a Janus. The importance and significance of our concept can be inspected from Fig. 1a, where our work is indicated with high novelty as well as great difficulty in actualization. Our sophisticated two-faced Janus metasurface enables four asymmetric *R* channels ($F_1\sim F_4$), with two generated at λ_1 and λ_2 along each face, see the schematic functions shown in Fig. 1b. Moreover, two symmetric *T* channels (F_5 & F_6) are naturally formed at λ_3 when a spin wave

impinges on the meta-plate from both sides. The high efficiency and elegant insulation among these channels are engineered by synthesizing triple R/T channels at each face with high-quality factor, see the inset shown in Fig. 1b, which calls on the elegant design of meta-atoms as further discussed below. Therein, we can engineer an arbitrarily predicted functionality by imposing desired phase patterns in each channel. Most importantly, we can further envision advanced functions for full-range scanning (full-space DOA) by integrating above channel-shifted versatile beams with progressive steering angles, or for large-capacity/complexity kaleidoscopic wavefronts by integrating channel-shifted hetero functions, facilitating large capacity, and great flexibility and versatility.

2. Methods

2.1 Chirality-assisted wavelength-space multitasking principle

To begin with, we first elaborate basic principle for wavelength-space multitasking, aiming to afford a solid platform and useful guideline for design. Suppose m wavelength/mode channels and n spatial port channels in our system, then a maximum of $m \times n$ information eigen-channels would be achieved. Here, the spatial port channel essentially refers to the main scattering directions in a full space. Intuitively, the information channels grow explosively if more DoFs will be involved, i.e., polarization, wavevector and incidence angle. However, more DoFs implies much more complicated system, which is more challenging in realization. The other tricky issue is how to simultaneously generate and individually manipulate these channels in a subwavelength scale without boosting the element footprint. More importantly, the elimination of the interferences among these modes is substantially crucial for individual control of both dynamic and geometric phases in each mode for advanced high-efficiency wave control. Here, to slightly relax the task but

not lose generality, we engineer six R and T channels across three wavelengths of a two-port system. A chirality strategy involving both in-plane and out-of-plane symmetry breaking was proposed to yield direction-encoded Janus functionalities and circumvent issues of mode interferences among boosted channels, which was previously employed only for polarization control [15],[39],[40], advancing a step over available applications.

2.2 Strategy and meta-atom design

As shown in Fig. 2a, the basic building block utilized for multitasking is a triple-layered thin meta-plate composed of a circular slotted patch sandwiched by two composite metallic structures in top-and-bottom sides. Two types of concentric sub-atoms are adopted to construct the composite pattern, say evolved H structure and dual-gap asymmetry split ring resonator (ASRR). The in-plane symmetry breaking of ASRR is facilitated by deviating one gap from the principal y axis by an angle of β while the other fixed. Such an asymmetry divides the ASRR into two counterparts with different resonant lengths, splitting the original mode into two (Fano effect [41]), see Supplementary Fig. S1. This proposal finds strong support from the differently localized current distributions on ASRR at λ_1 and λ_2 (Supplementary Fig. S2). The isotropic patch with a centric circular slot etched in the middle layer behaves as a ground plane and thus assists ASRR to afford two R modes at λ_1 and λ_2 . In contrast, it functions as a spatial mode filter and is accompanied with evolved H structure to form an ABA-like T mode at λ_3 . Besides, the full-fold rotational symmetry of the circular ring shares different orientations of ASRR and evolved H, and thus facilitates both R and T geometric phases with perfect insulation. The out-of-plane symmetry breaking is engineered by designing the two-faced ASRRs with different structures and orientations, yielding direction-encoded distinct R phase patterns in analog to a Janus.

Typically, we choose chessboard configuration instead of concentric distribution of ASRR and evolved H along a shared optical axis to completely insulate the coupling for individual control^[33]. Quite interestingly, the strong field localization of utilized evolved H in a thin profile enables large quality factor (Supplementary Fig. S2) which is very beneficial for suppressing the mutual interference. Although increasing the vertical thickness between top and bottom layer enhances the bandwidth occasionally, it yet destroys the high concentration of fields around ASRR and evolved H, which is the key for mode insulation. Plus appropriate mode interval, the encapsulation of evolved H in ASRR guarantees simultaneously independent control and subwavelength scale. The mode interval ($\rho=f_2/f_1$) can be arbitrarily engineered by tuning the position of the asymmetric gap (angle β). Large β would lead to large ρ (lower f_1 and higher f_2), i.e., $\rho=1.4$ at $\beta=30^\circ$, and $\rho=1.78$ at $\beta=50^\circ$, see Supplementary Fig. S2. Such a mechanism completely distinguishes our strategy from available harmonic approach^[42] or merging concept^{[19]-[22]}. Finally, the high efficiency of spin conversion for triple R and T modes is well engineered by controlling the dynamic amplitudes and phases of the anisotropic ASRR and evolved H in both orthogonal LP polarizations to fulfill the condition of $|r_{yy}|\approx|r_{xx}|\approx 1$, $|t_{yy}|\approx|t_{xx}|\approx 1$, and $|\phi_{yy}-\phi_{xx}|\approx\pi$, see Supplementary Fig. S3.

Given the clear physics for triple-mode and high-efficiency operation, it is readily to finalize the design by carefully considering the mode interval. Here, we engineer a meta-atom with $f_1=7.4$, $f_2=9.1$ and $f_3=12.3$ GHz. As is much appreciated from Figs. 2b~2d, individual change of ψ_1 and ψ_3 within $0\sim 150^\circ$ in steps of 30° induces elegant R/T geometric phase at f_1, f_2 and f_3 without significant phase distortion, indicating a satisfactory suppressed mutual impact. Such a proposal further finds strong support from the blue curve, where altering ψ_2 in the backward does not pose any influence on the R/T response at forward side. The undistorted dual- R geometric phase as a function of $2\psi_1$ is

quite physical because a sharp 180° phase jump occurring between f_1 and f_2 . Beyond the exception point, near perfect geometric phase is observed (Figs. 2b~2d and Supplementary Figs. S4-S6). The individual control of R/T modes in both sides can be further evidenced from the negligible mode shift and amplitude penalty at f_1 , f_2 and f_3 in full spectrum when altering ψ_1 , ψ_2 and ψ_3 (see Supplementary Figs. S4~S6). These inspected features are also expected from the opposite side of the meta-atom (backward channel) in a completely independent manner. Above elegant isolation among six channels is the key for engineering asymmetry forward and backward functions of $F_1\sim F_6$ in both sides. Most importantly, the near-unity spin conversion is inspected in all R/T modes, which is very promising for high-efficiency metadevices. In the following, we will devise two metadevices to demonstrate our wavelength-space multitasking concept and uncover its possible applications. The triple-layer metallic patterns of each metadvice are fabricated individually on two dielectric boards using printed-circuit-board technique. They were assembled together through adhesives and reinforced through a hot, and finally experimentally characterized through both near-field and far-field measurements, see Supplementary Information (section 5)

3. Results and discussion

3.1 Large-scanning kaleidoscopic-beam generator

Highly-directive multi-beam emission system with large cover especially for a full-space span promises great potentials in radar, satellite-based communication, SAR, smart antenna, and multiple-input multiple-output systems. However, available approaches typically require a complicated beam-forming network. Here, we devised and characterized a passive metadvice that is capable of manifesting kaleidoscopic beams for full-space DOA without any network. Such an advanced large-scanning capability is unbelievable before our wavelength-space concept and

distinguishes completely from current anisotropic scheme capable of manipulating EM wave in two reflection channels under dual-orthogonal LP ^{[43]-[45]} and spin waves ^{[23]-[26]}. The compound plate is predesigned with six spatial wavevectors covering both principal planes and directing at $(\Phi, \theta)=(0^\circ, 30^\circ)$, $(0^\circ, 24^\circ)$, $(90^\circ, 151^\circ)$, $(90^\circ, 222.5^\circ)$, $(90^\circ, 212.5^\circ)$, and $(90^\circ, 331^\circ)$ under σ_+ wave. This can be accomplished by imparting six distinct wavevectors () into the forward and backward R/T channels according to $\sin \theta_{r/t} = \frac{\xi}{k_0} = \frac{\lambda}{\Gamma}$, where Γ is the period with 2π phase cover.

Plus the wavelength and space multitasking, here we only require three linear gradients (eight, six and five meta-atoms in a supercell) by spatially rotating the top-and-bottom ASRR (ψ_1 and ψ_2) and dual-layer evolved H (ψ_3), see phase patterns and metasurface layout depicted in Figs. 3(a), 3(c) and Supplementary Fig. S7. Then, the resulting reflection/deflection angles $\theta=\sin^{-1}(\xi/k_0)$ can be readily predicted as a function of ξ according to the generalized Snell's law ^[2]. As is expected in Fig. 3(b), six spatial beams with two and four wavevectors are clearly inspected across $\Phi=0^\circ$ and $\Phi=90^\circ$ plane in full space from both numerical and experimental far-field patterns. The beam-steering property can be further evidenced from the near-field E_{σ_+} or E_{σ_-} patterns shown in Fig. 3(e), where oblique planar wavefront is clearly inspected. Most importantly, these wavevectors are precisely directed along target angles predicted by theory with an angle error of $\pm 1^\circ$ (Fig. 3d), indicating negligible interference among these well-insulated channels. The FDTD calculated and measured efficiency evaluated as the ratio between the powers carried by the reflected/refracted beam and the total power integrated over full space is more than 92%/84% in all six $R-T$ channels. The slightly reduced efficiency in experiment case is attributable to the higher sidelobes induced by the slightly distorted phase patterns. Such level of high-efficiency and advanced full-space scanning is

extremely difficult for an active phased array, not to mention the existing passive metasurfaces [29][32] for high-efficiency spin conversion at one single R or T channel.

3.2 Wide-angle large-capacity reverser

In the following, we demonstrated another more advanced function, called a reverser, by using our Janus metasurface, which enables to reverse predefined in-plane components of momentum in both R (retroreflector) and T (negative refractor) channels. Such an integrated reverser can be considered as another alternative for full-space DOA. Retroreflector is an important device in the discipline of navigation safety, target labeling, RCS/visibility enhancement, remote sensing and satellite communication. It allows the reflection of the EM wave propagating back along its oblique incident direction. Available approaches such as corner reflector and Luneburg lens have been reported, however, the bulk size, large weight and nonplanar configuration have hindered its real-world applications since it does not meet the native compatibility for integration and miniaturization. Employing metasurface for such a task has been an intriguing issue most recently [46]-[50], especially for the adaptive retroreflector, which is only demonstrated by mechanically altering the geometry of reconfigurable C-shaped resonators [48] or switchable metagrating [49]. Nevertheless, large-angle retroreflection particularly in full space is still extremely challenging for a passive metasurface, not to mention the proposed compound large-capacity reverser which promises great potential applications in multi-target tracking. Here, we engineer a full-space reverser that integrates retroreflection at f_1 and f_2 and negative refraction at f_3 inspired by our wavelength-space multitasking concept. More importantly, the retroreflections at f_1 and f_2 in forward and backward channels can be independently modulated, see Fig. 4a.

The design of retroreflector origins from the conservation of tangential momentum in the

transverse plane. To flip the in-plane component of the momentum of incident light (\mathbf{p}_{\parallel}), we need to impart an exact momentum ($\mathbf{p}_m = -2\mathbf{p}_{\parallel}$) on the gradient metasurface for compensation, which follows the condition $\sin \theta_i - \sin \theta_{r/t} = 2 \sin \theta_i = \frac{\xi}{k_0} = \frac{\lambda}{T}$. Therefore, the reflective and transmissive phase patterns of the full-space retroreflector should fulfil $\varphi_{\theta_i} = \frac{4\pi}{\lambda}(n-1)p \sin \theta_i$, where n is the total number of meta-atoms along transverse direction. To engineer a multispectral retroreflector and negative refractor at large incidences, we require that the EM response, especially the manifested phase of the meta-atom is insensitive to the incident angle θ_i .

To begin with, we first evaluate the angle-immune EM response of the composite meta-atom to θ_i , as shown in Fig. 2e and Supplementary Fig. S8. The R/T spin-conversion coefficients in all channels deteriorate slightly as θ_i increases. Nevertheless, all intensity is inspected more than 0.9 at f_1, f_2 and f_3 even at $\theta_i = 60^\circ$. Moreover, the phase response is preserved almost constant at three target bands (grey region) despite slight deviation at off-resonant frequencies at $\theta_i = 60^\circ$. All inspected phenomenon reveals an elegant angle-immune EM response which is essentially important for a retroreflector at large incidence angle. Similar angle-insensitive EM property can be also expected when the incidence is along yz plane, see Supplementary Fig. S9. More interestingly, the symmetry-breaking in ASRR is beneficial for the incidence-angle insensitivity, see EM response of the SRR meta-atom without symmetry-breaking portrayed in Supplementary Fig. S10, where a sharp reflection dip with amplitude and phase fluctuations appears when $\theta_i \neq 0^\circ$. The physics behind the angle-immune behaviour of ASRR is because similar electric and magnetic dipole modes are excited with stable intensity for different θ_i .

The integrated multitasking retroreflector and negative refractor is predesigned at both sides of the metasurface for both R/T channels, see the schematic functionality shown in Fig. 4a. Here, the

negative refraction (nega-refraction) occurs at T channel without mirror longitudinal momentum since the outgoing wave manifests reversed tangential momentum (in analogue to retroreflection) and thus maintains at the same side of the normal. The multitasking metadvice is capable of retroreflecting the σ^- wave at θ_1 and θ_2 in the forward channel, whereas it enables to reflect back the σ^+ wave at θ_3 and θ_4 in the backward channel. Moreover, the nega-refraction angle is engineered toward θ_5 and $-\theta_5$ at $-\theta_5$ and θ_5 in the forward and backward side, respectively. Given the integrated functions and our sophisticated approach, we can immediately synthesize the required phase patterns in six channels (see Fig. 4b). By imposing these theoretically calculated phase profiles, it is readily to figure out the final metadvice layout shown in Fig. 4c and Supplementary Fig. S11. Figs. 4d and 4e show the FDTD calculated and experimental results of the far-field scattering intensity of our designed multiplexed full-space retroreflector. As is expected in Fig. 4d, a reasonable agreement is appreciated in all six channels except for a minor angle deviation of only $\pm 1.5^\circ$ between FDTD and experimental results. Such minor deviation may be attributed to the adhesives introduced in the tri-layer sample fabrication and tolerances inherent in measurements. From Fig. 4e, we clearly observe six outgoing waves whose tangential momentum is in reverse to its original incident one at six angles of $\theta_i = -30^\circ, -22.7^\circ, -40^\circ, 20^\circ, 15.3^\circ, \text{ and } 40^\circ$ along both forward and backward channels of the metadvice. The overall efficiency is more than 91% in all measured retroreflection cases, except for 76% and 75% at $\theta_i = \pm 40^\circ$ which is very comparable to the available reports of large-angle transmission. Moreover, the large angle operation of our retroreflector is very intriguing with respect to the available report which is confined to 20° [48]. Finally, the released DoF indicates that we can also engineer achromatic retroreflector and nega-refractor in the same incidence at f_1 and f_3 .

4. Conclusions

To sum up, we have proposed yet demonstrated the wavelength-space multiplexed Janus metasurface concept with high capacity, high efficiency and extraordinary DoFs by involving both in-plane and out-of-plane symmetry breaking. The spin-encoded metasurface enables the simultaneous control of R and T wavefronts not only with two-faced distinct functions but also in multiple wavelengths. Two multitasking metadevices are devised for extreme wave control, one exhibiting kaleidoscopic beams for large-range scanning, and the other integrating retroreflection and negative refraction for wide-angle operation. Numerical and experimental results have both shown the predicted functionality with desired efficiency of more than 75% for all six channels. The advanced functionality realized for kaleidoscopic beam scanning in full space goes far beyond previous attempts for unitary anomalous refraction and retroreflection. Our strategy, features extraordinary capacity, ultrathin profile with a thickness of only $\lambda_1/21$, large-angle and full-space operation, promising great potential in integrated thin optics with kaleidoscopic functions.

Acknowledgements

Not applicable.

Authors' contributions

H-XX conceived the idea of the wavelength-space multitasking Janus metasurfaces, theoretically designed and fabricated the samples, and performed the FDTD simulations. H-XX, YW, CW, MW and SW conducted the experiments. GH, ST, YH and XL analyzed the results and made additional

efforts in preparing the manuscript. H-XX wrote the manuscript with input from all authors. C-WQ and WH supervised the project. All authors discussed the results and commented on the manuscript.

Funding: This work was supported by the National Defense Foundation of China (2019-JCJQ-JJ-081); the Youth Talent Lifting Project of the China Association for Science and Technology (17-JCJQ-QT-003); the Key Program of Natural Science Foundation of Shaanxi Province (2020JZ-33); the Key Principal's Fund of Air Force Engineering University (XNLX19030601); the National Key Research and Development Program of China (Grant NO. 2017YFA0700202); the National Natural Science Foundation of China (61701082).

Availability of data and materials

The data that support the findings of this study are available from the corresponding author on request.

Competing interests

The authors declare that they have non-financial competing interests.

References

- [1] Josefsson L and Persson P. Conformal array antenna theory and design. NJ: IEEE Press; 2006.
- [2] Yu N and Gaburro Z. Light Propagation with phase discontinuities: generalized laws of reflection and refraction. *Science*. 2011; 334: 333–7.
- [3] Shaltout AM, Shalaev VM and Brongersma ML. Spatiotemporal light control with active metasurfaces. *Science*. 2019; 364: 648–57.
- [4] He Q, Sun SL and Zhou L. Tunable/Reconfigurable Metasurfaces: Physics and Applications. *Research*. 2019; 1849272
- [5] Ding F, Pors A and Bozhevolnyi SI. Gradient metasurfaces: a review of fundamentals and applications. *Reports on Progress in Physics*. 2018; 81: 44.
- [6] Zhao J, Yang X and Dai J Y, et al. Programmable time-domain digital-coding metasurface for non-linear harmonic manipulation and new wireless communication systems. *National Science Review*. 2019; 6: 231-8.
- [7] Iyer AK, Alu A and Epstein A. Metamaterials and Metasurfaces-Historical Context, Recent Advances, and Future Directions. *IEEE Trans. Antennas Propag.* 2020; 68: 1223–31.
- [8] Huang YW, Xu HX and Sun S, et al. Structured semiconductor interfaces: active functionality on light manipulation. *Proceedings of IEEE*. 2020; 108: 772–94.
- [9] Xu HX, Tang S and Wang GM, et al. Multifunctional microstrip array combining a linear polarizer and focusing metasurface. *IEEE Trans. Antennas Propag.* 2016; 64: 3676–82.
- [10] Cai T, Wang G and Tang S, et al. High-efficiency and full-space manipulation of electromagnetic wave fronts with metasurfaces. *Physical Review Applied*. 2017; 8: 034033.
- [11] Zhang L, Wu RY and Bai GD, et al. Transmission-reflection integrated multifunctional coding metasurface for full-space controls of electromagnetic waves. *Adv. Funct. Mater.* 2018; 28: 1802205.
- [12] Wu RY, Zhang L and Bao L, et al. Digital metasurface with phase code and reflection-transmission amplitude code for flexible full-space electromagnetic manipulations. *Adv. Opt. Mater.* 2019; 7: 1801429.
- [13] Yang J, Wu X and Song J, et al. Cascaded metasurface for simultaneous control of transmission and reflection. *Optics Express*. 2019; 27: 9061–70.
- [14] Zhang X, Pu M and Guo Y, et al. Colorful metahologram with independently controlled images in transmission and reflection spaces. *Adv. Funct. Mater.* 2019; 29: 1809145.
- [15] Chen K, Ding GW and Hu GW, et al. Directional Janus Metasurface. *Advanced Materials*. 2020; 32: 1906352.
- [16] Huang C, Pan WB, Ma XL, et al. Multi-spectral metasurface for different functional control of reflection waves. *Scientific Reports*. 2016; 6: 23291.
- [17] Arbabi E, Arbabi A and Kamali SM, et al. Multiwavelength polarization-insensitive lenses based on dielectric metasurfaces with meta-molecules. *Optica*. 2016; 3: 628–33.
- [18] Ding J, An S, Zheng B and Zhang H. Multiwavelength metasurfaces based on single-layer dual-wavelength meta-atoms: toward complete phase and amplitude modulations at two wavelengths. *Adv. Opt. Mater.* 2017; 5: 1700079.
- [19] Aieta F, Kats MA, Genevet P and Capasso F. Multiwavelength achromatic metasurfaces by dispersive phase compensation. *Science*. 2015; 347: 1342–45.
- [20] Zhou Y, Kravchenko II and Wang H, et al. Multilayer noninteracting dielectric metasurfaces for multiwavelength

metaoptics. *Nano Lett.* 2018; 18: 7529–37.

- [21] Bai GD, Ma Q and Iqbal S, et al. Multitasking shared aperture enabled with multiband digital coding metasurface. *Adv. Opt. Mater.* 2018; 6: 1800657.
- [22] Xu HX, Zhang L and Kim Y, et al. Wavenumber-splitting metasurfaces achieve multi-channel diffusive invisibility. *Adv. Opt. Mater.* 2018; 6: 1800010.
- [23] Mueller JPB, Rubin NA and Devlin RC, et al. Metasurface polarization optics: independent phase control of arbitrary orthogonal states of polarization. *Phys. Rev. Lett.* 2017; 118: 113901.
- [24] Devlin RC, Ambrosio A and Rubin NA, et al. Arbitrary spin-to-orbital angular momentum conversion of light. *Science.* 2018; 358: 896–901.
- [25] Xu HX, Han L and Li Y, et al. Completely spin-decoupled dual-phase hybrid metasurfaces for arbitrary wavefront control. *ACS Photonics.* 2019; 6: 211–20.
- [26] Ding G, Chen K and Luo X, et al. Direct routing of intensity-editable multi-beams by dual geometric phase interference in metasurface. *Nanophotonics.* 2020; 20200203.
- [27] Zhang K, Yuan YY, Ding XM, Ratni B., Burokur SN, and Wu Q. High-efficiency metalenses with switchable functionalities in microwave region. *ACS Appl. Mater. Interfaces.* 2019; 11: 28423.
- [28] Li Z, Liu W and Cheng H, et al. Spin-selective full-dimensional manipulation of optical waves with chiral mirror. *Adv. Mater.* 2020; 32: 1907983.
- [29] Xu HX, Hu G and Li Y, et al. Interference-assisted kaleidoscopic meta-plexer for arbitrary spin-wavefront manipulation. *Light: Sci. Appl.* 2019; 8: 3.
- [30] Luo W J, Sun S L, Xu HX, et al. Transmissive ultra-thin Pancharatnam–Berry metasurfaces with nearly 100% efficiency. *Physical Review Applied.* 2017; 7: 044033.
- [31] Yin X, Ye Z, Rho J, et al. Photonic spin hall effect at metasurfaces. *Science.* 2013; 339: 1405.
- [32] Luo W, Xiao S, He Q, et al. Photonic spin hall effect with nearly 100% efficiency. *Adv. Opt. Mater.* 2015; 3: 1102.
- [33] Xu HX, Hu G and Jiang M, et al. Wavevector and frequency multiplexing performed by a spin-decoupled multichannel metasurface. *Adv. Mater. Technol.* 2019; 5: 190071.
- [34] Cai T, Wang G and Xu HX, et al. Bifunctional pancharatnam-berry metasurface with high-efficiency helicity-dependent transmissions and reflections. *Annalen der Physik.* 2018; 530: 1700321.
- [35] Zhang C, Wang G, et al. Helicity-dependent metasurfaces for wave control. *Adv. Opt. Mater.* 2020; 8: 1901619.
- [36] Hu G, Hong X, Wang K, et al. Coherent steering of nonlinear chiral valley photons with a synthetic Au–WS₂ metasurface. *Nature Photonics.* 2019; 13: 467–72.
- [37] Jin L, Dong Z and Mei S, et al. Noninterleaved metasurface for (2⁶-1) spin- and wavelength-encoded holograms. *Nano Lett.* 2018; 18: 8016-24.
- [38] Jin L, Huang Y and Jin Z, et al. Dielectric multi-momentum meta-transformer in the visible. *Nat. Commun.* 2019; 10: 4789.
- [39] Liu C, Bai Y and Zhou J, et al. High-performance bifunctional polarization switch chiral metamaterials by inverse design method. *NPJ Computational Materials.* 2019; 5: 93.
- [40] Xu HX, Hu G and Han L, et al. Chirality-assisted high-efficiency metasurfaces with independent control of phase, amplitude and polarization. *Adv. Opt. Mater.* 2019; 7: 1801479.
- [41] Luk'Yanchuk B, Zheludev NI and Maier SA, et al. The Fano resonance in plasmonic nanostructures and metamaterials. *Nat. Mater.* 2010; 9: 707–15.

-
- [42] Zhang L, Chen XQ and Liu S, et al. Space-time-coding digital metasurfaces. *Nat. Commun.* 2018; 9: 4334.
- [43] Xu HX, Tang S and Ling X, et al. Flexible control of highly-directive emissions based on bifunctional metasurfaces with low polarization cross-talking. *Annalen Der Physik.* 2017; 529: 1700045.
- [44] Liu S, Cui TJ and Noor A, et al. Negative reflection and negative surface wave conversion from obliquely incident electromagnetic waves. *Light: Sci. Appl.* 2018; 7: 11.
- [45] Zhang XG, Yu Q and Jiang WX, et al. Polarization-controlled dual-programmable metasurfaces. *Adv. Sci.* 2020; 7: 1903382.
- [46] Arbabi A, Arbabi E and Horie Y, et al. Planar metasurface retroreflector. *Nat. Photon.* 2017; 11: 415.
- [47] Ra'di Y, Sounas DL and Alù A. Metagratings: beyond the limits of graded metasurfaces for wave front control. *Phys. Rev. Lett.* 2017; 119: 067404.
- [48] Yan L, Zhu W and Karim MF, et al. $0.2 \lambda_0$ thick adaptive retroreflector made of spin-locked metasurface. *Adv. Mater.* 2018; 30: 1802721.
- [49] Li M, Jing LQ and Lin X, et al. Angular-adaptive spin-locked retroreflector based on reconfigurable magnetic metagrating. *Adv. Opt. Mater.* 2019; 7: 8.
- [50] Wong AMH, Christian P and Eleftheriades GV. Binary Huygens' metasurfaces: experimental demonstration of simple and efficient near-grazing retroreflectors for TE and TM polarizations. *IEEE Trans. Antennas Propag.* 2018; 66: 2892–903.

Figures and tables

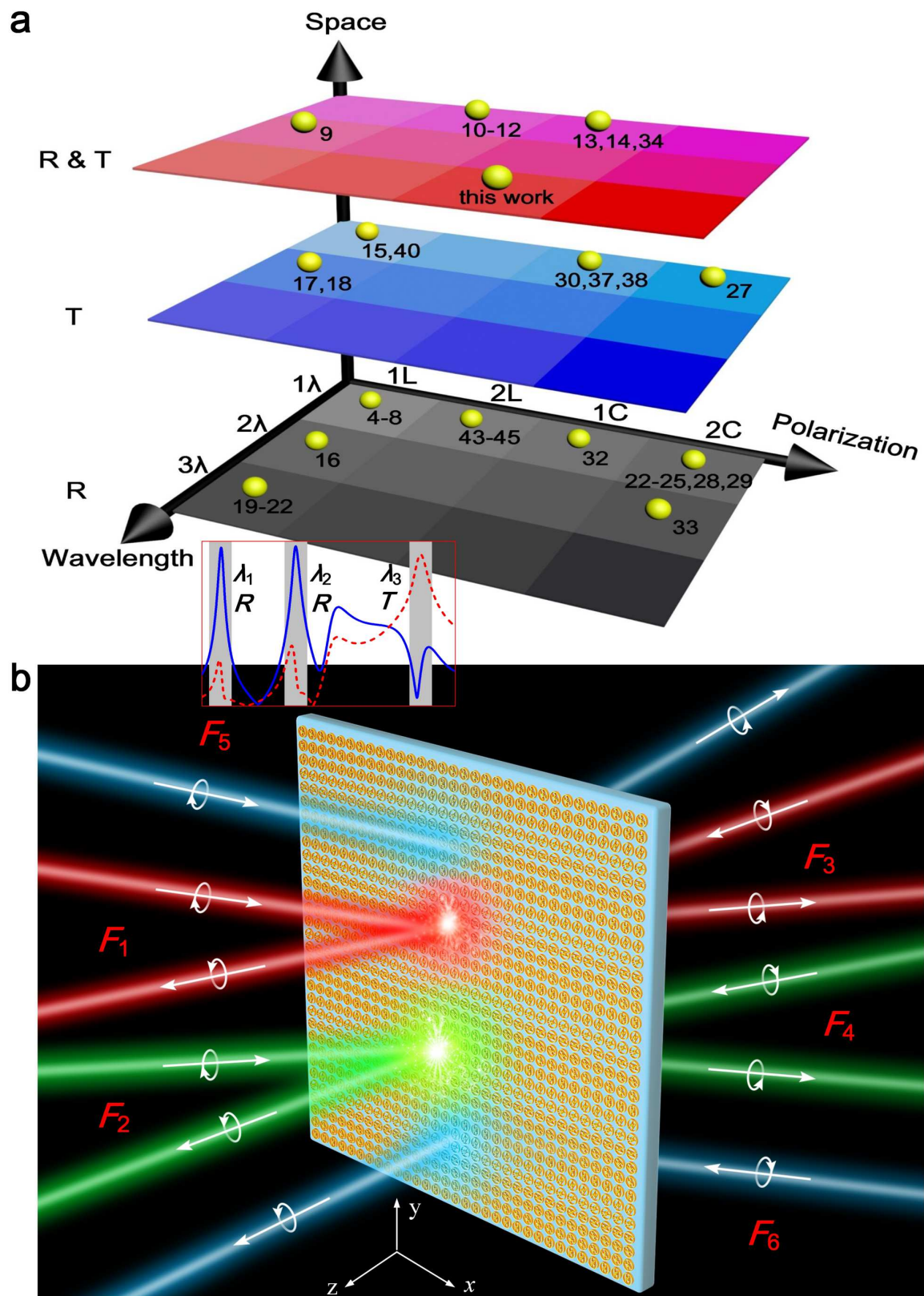


Figure 1. Illustration of the (a) evolution and (b) advanced function of our wavelength-space multitasking Janus metasurface concept for kaleidoscopic full-space spin-wave control. To clearly

show the evolutionary process of proposed concept, we summarize existing metasurfaces for EM wave manipulation in a three-dimensional coordinate system indicated by three information axes of space, wavelength and polarization. Here, the yellow sphere indicating available work with reference numbers marked besides and the gradient panel from light to dark represents the degree of difficulty in realization. The L and C indicate linear and circular polarization (CP), 2L and 2C mean two orthogonal LP and CP wave operations, and R and T indicate reflection and transmission, respectively. Note that the high-efficiency CP operation indicated here requires specific condition of dynamic phases of two orthogonal LP components under LP wave excitations and thus is more difficult than dual-LP operation. Three colours in schematic function represent three synthesized spectrum channels at different operation wavelengths of λ_1 , λ_2 and λ_3 while different angles of each outgoing wave indicate full-space DOA or integrated large-capacity functionalities.

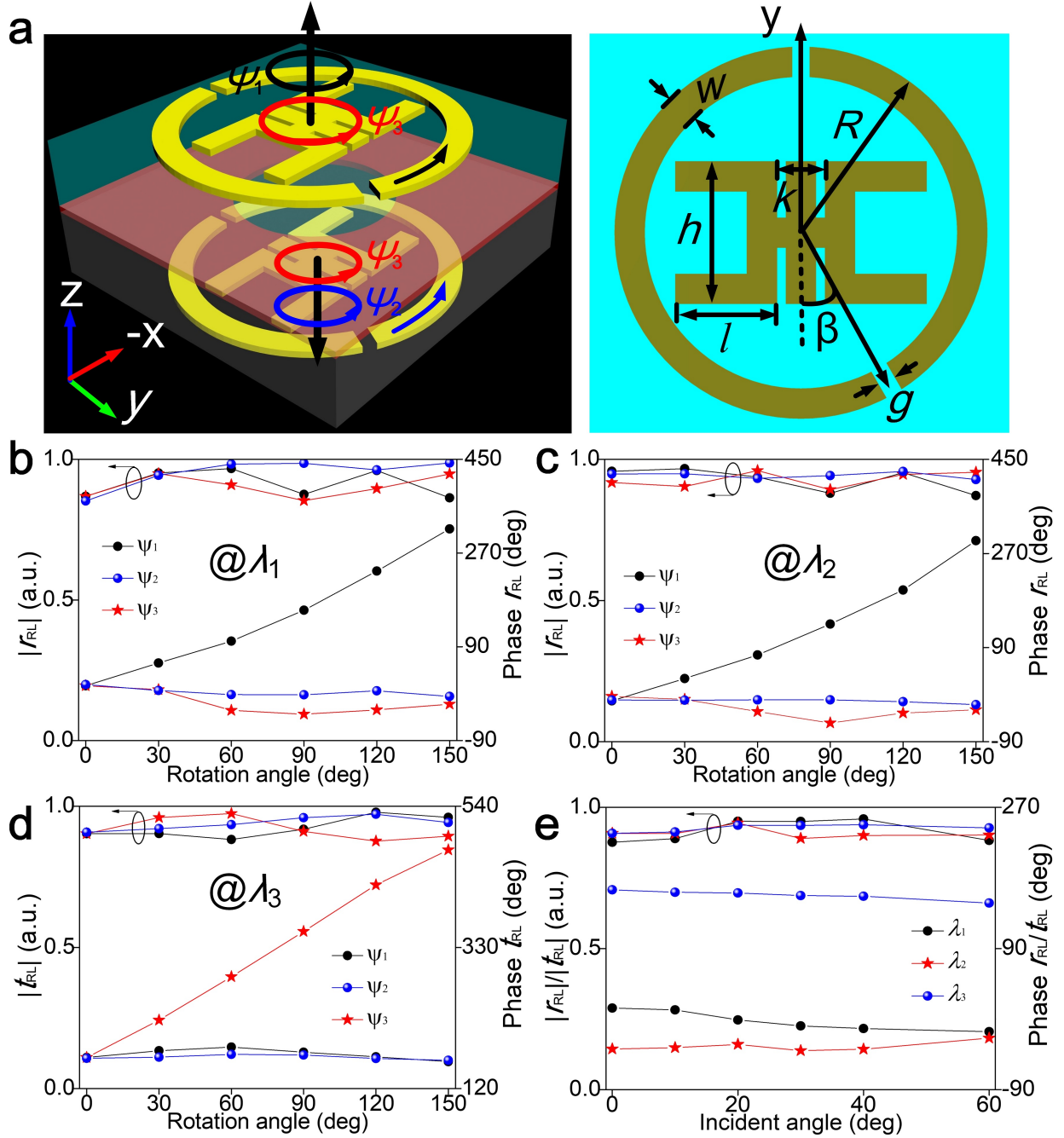


Figure 2. Characterization of the composite meta-atom for wavelength-space multitasking when the EM wave illuminates from the forward side. Similar results and conclusion can be drawn in backward case. Here, both dynamic and geometric phases are utilized to construct the predesigned functions with high efficiency by rotating each of well-designed sub-atoms along its central axis, for example the orientation of the top and bottom ASRR (ψ_1 and ψ_2) and the entire dual-layer evolved H (ψ_3). (a) Layout and parametric illustration, here, detailed structure parameters are $p_x=p_y=10$, $k=1.4$, $h=3$, $l=2.2$, $w=0.4$, $g=0.4$, $R=4.15$ mm, $\beta=20^\circ$ and the radius of circular slot in middle layer is 2.3 mm. The commonly available F4B board with a dielectric constant $\epsilon_r=2.65$, loss

tangent $\tan\delta=0.001$, and thickness $h=1$ mm is utilized as the dielectric spacer. Effects of ψ_1 , ψ_2 and ψ_3 to the spin-conversion reflection r_{RL} at (b) λ_1 , (c) λ_2 and to the spin-conversion transmission t_{RL} at (d) λ_3 . (e) The angle-immune EM response (r_{RL} at λ_1 , λ_2 and t_{RL} at λ_3) of the composite meta-atom as a function of θ_i . Here, the left and right scale is plotted for amplitude and phase, respectively.

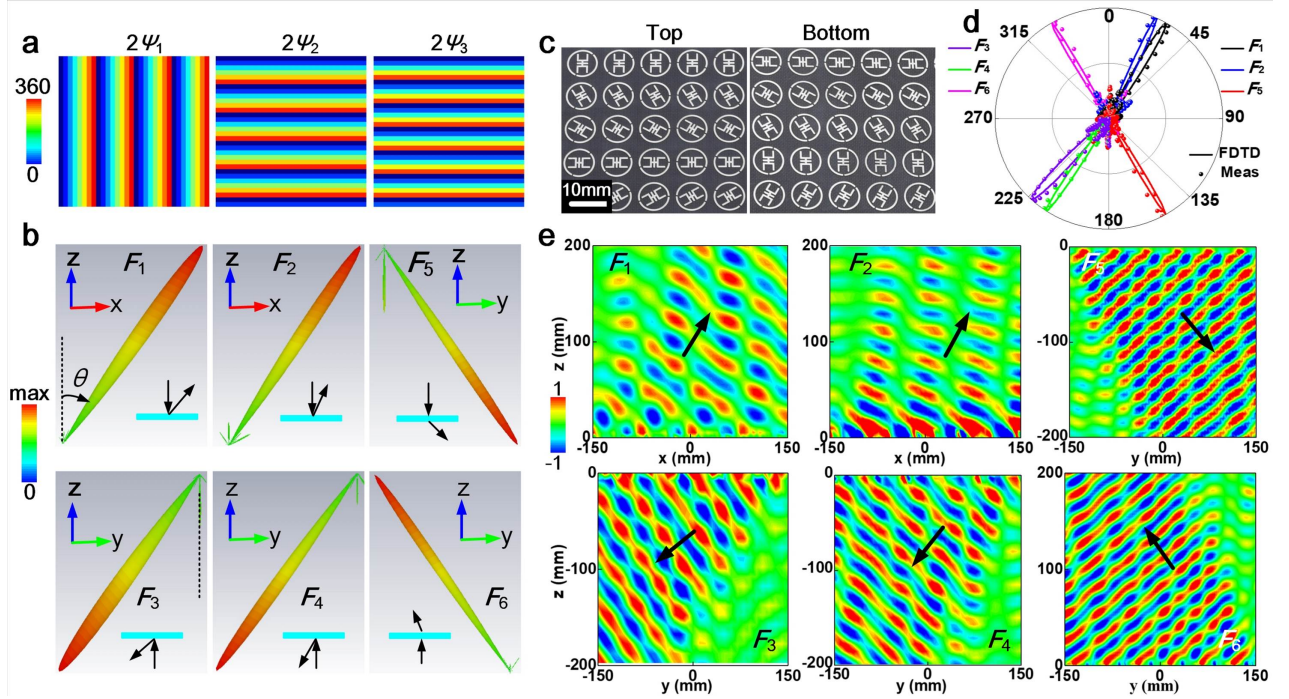


Figure 3. Characterization of the multitasking kaleidoscopic-beam generator for full-space DOA comprising 32×32 meta-atoms and occupying an area of 320×320 mm². (a) Required phase distributions in 2D profile (top panel) and along centre line (bottom panel). Three types of phase gradients $\zeta=2\pi/np$ imposed along x and y directions of each forward or backward channel with n the number of meta-atoms in a supercell (here n is 8, 6 and 5 for ζ_1 , ζ_2 and ζ_3 , respectively). (b) FDTD calculated FF scattering patterns for functions of $F_1 \sim F_6$. (c) Zoom-in view of the fabricated sample. (d) Comparison of FF scattering cross-section intensity between FDTD calculations and experiments. (e) Experimentally measured NF patterns (E field) in xz and yz planes.

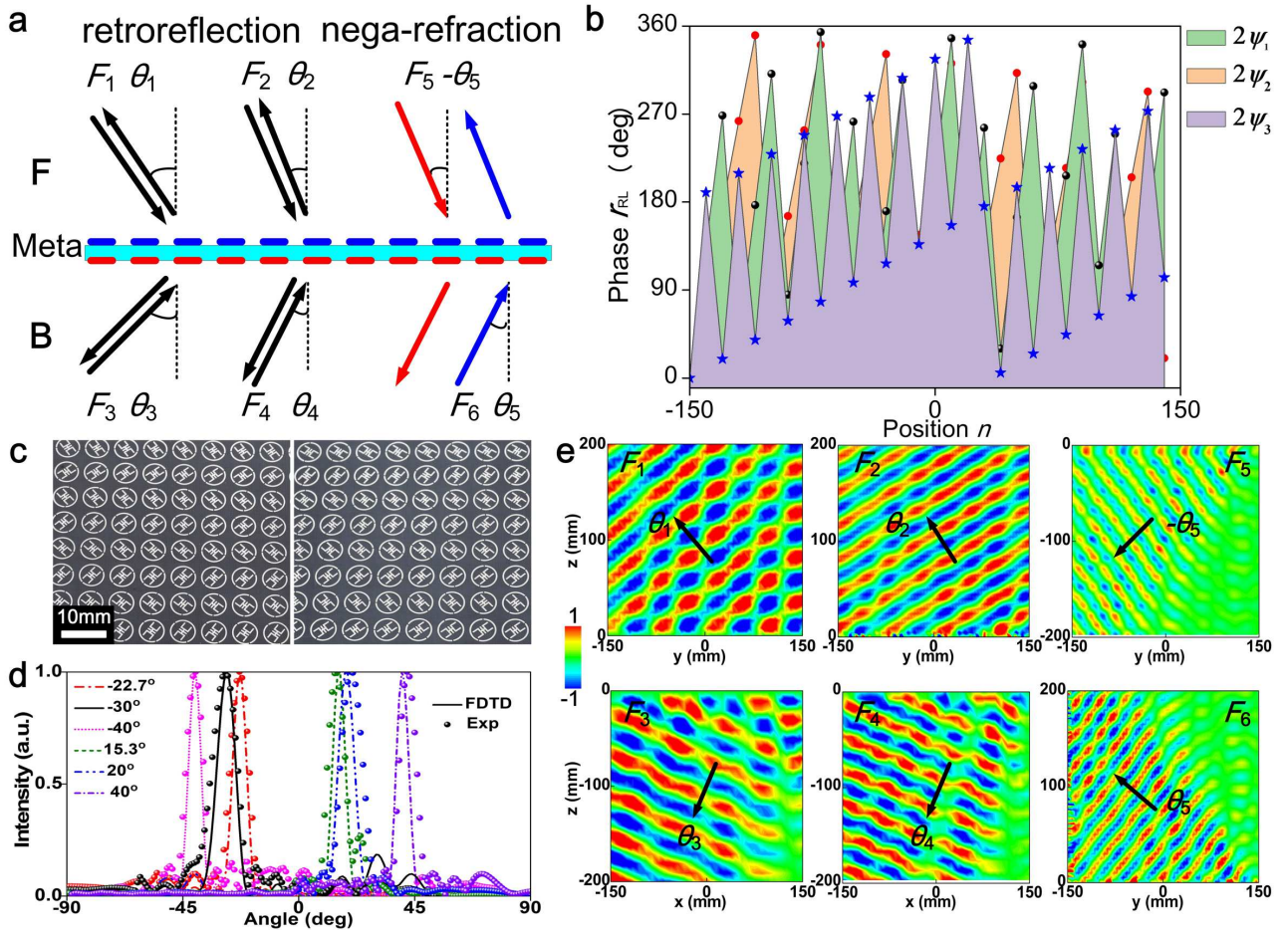


Figure 4. Characterization of the multitasking reverser (integrated retroreflector and negative refractor) for full-space DOA comprising 30×30 meta-atoms and occupying an area of 300×300 mm². (a) Illustration of the schematic functionality. (b) Required phase distributions in 2D profile (top panel) and along centre line (bottom panel). (c) Zoom-in view of the fabricated sample. (d) Comparison of FF scattering cross-section intensity between FDTD calculations and experiments. (e) Experimentally measured NF patterns (E field) in xz and yz planes for functions of $F_1\sim F_6$. Here, the reflection or refraction angle is defined with respect to the normal within $-90^\circ\sim 90^\circ$ and all measured results intensity are normalized against its maximum.

Supplementary Information

Spin-encoded wavelength-space multitasking Janus metasurfaces

By He-Xiu Xu^{1,2,6*}, Chaohui Wang¹, Yanzhao Wang¹, Mingzhao Wang¹, Shaojie Wang¹, Guangwei Hu³, Shiwei Tang⁴, Yongjun Huang⁵, Xiaohui Ling⁶, Wei Huang^{2*}, Cheng-Wei Qiu^{3*}

¹*Air and Missile Defense College, Air Force Engineering University, Xi'an 710051, China*

²*School of Natural and Applied Sciences, Northwestern Polytechnical University, Xi'an 710072, China*

³*Department of Electrical and Computer Engineering, National University of Singapore, Singapore 117583, Singapore*

⁴*Department of Physics, Faculty of Science, Ningbo University Ningbo 315211, China*

⁵*School of Information and Communication Engineering, University of Electronic Science and Technology of China, Chengdu 611731, China*

⁶*College of Physics and Electronic Engineering, Hengyang Normal University, Hengyang 421002, China*

- 1. FDTD calculations**
- 2. Additional results for the composite meta-atom**
- 3. Layout of the large-scanning kaleidoscopic-beam generator**
- 4. Angle-insensitive performance for wide-angle large-capacity reverser**
- 5. Fabrication and experimental setup**

1. FDTD calculations

All numerical designs and characterizations are performed through FDTD simulations based on a commercial software package. Specifically, the reflection/transmission amplitudes/phases are obtained by studying a single meta-atom with periodic conditions imposed at its four boundaries and a Floquet port assigned at a distance of 15 mm away from the xy-plane where the meta-atom is placed. In the far-field and near-field calculations, we characterized the two entire metadevices consisting of 32×32 and 30×30 meta-atoms, with open boundary conditions set at its four boundaries in the xy-plane. In all cases, the metadvice/meta-atom is illuminated by normally incident LCP and RCP plane wave.

2. Additional results for the composite meta-atom

The frequency ratio (f_2/f_1) between two R modes can be progressively controlled by adjusting the position of the asymmetry gap (angle β), see Fig. S1. As can be seen, large β would lead to large frequency interval/ratio, namely, lower f_1 and higher f_2 . Moreover, the efficiency slightly deteriorates when β increases. Nevertheless, we obtain a high efficiency of more than 0.91 and a frequency ratio of 1.4 ($f_1=7$ and $f_2=9.8$ GHz) at $\beta=30^\circ$, and a larger frequency ratio of 1.78 ($f_1=6.5$ and $f_2=11.6$ GHz) at $\beta=50^\circ$.

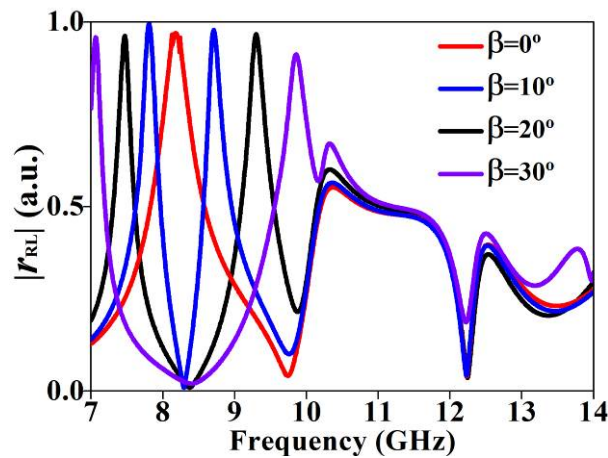


Figure S1 Illustration of the frequency ratio control over f_1 and f_2 by the asymmetry gap β .

To gain an insight into the principle of multiband operation, we afford FDTD calculated current distributions on the meta-atom, see Fig. S2. As can be inspected, the current is densely distributed around the left longer part of ASRR at f_1 , whereas it is strongly localized around the right shorter part at f_2 , accounting for the two reflective operation band. Moreover, the current intensity is mainly concentrated near the top-and-bottom evolved H patterns and centre annular slot at f_3 , indicating an ABA transmission response. The origin of above three operation modes gives us a clear guideline for individual control.

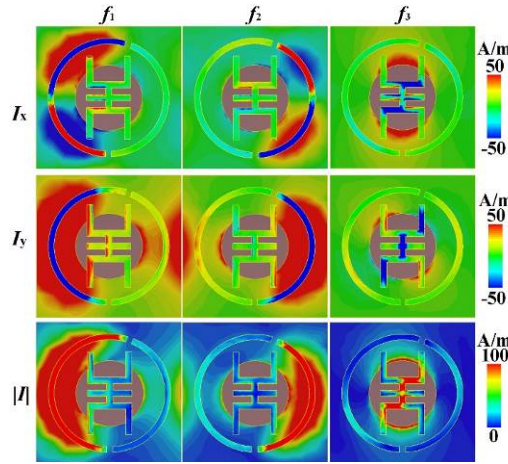


Figure S2 Current distributions on the meta-atom at three representative frequencies of f_1 , f_2 and f_3 .

Given the clear origin of three resonances, the key for meta-atom design is how to maintain the high efficiency of spin conversion. Fig. S3 plots the frequency spectrum of the composite meta-atom under x and y linearly-polarized (LP) EM wave excitation for both reflection and transmission, respectively. As is appreciated, high reflection rate ($|r_{yy}| \approx |r_{xx}| > 0.88$) and transmission ($|t_{yy}| \approx |t_{xx}| \approx 1$) rate are clearly observed at f_1 , f_2 , and f_3 for both co-polarized components in two cases. Moreover, the phase difference ($\varphi_{yy} - \varphi_{xx}$) between them is around 180° across three bands. Therefore, we conclude that the high spin conversion efficiency can be well engineered by controlling birefringent response of the anisotropic ASRR and evolved H structure under LP excitation.

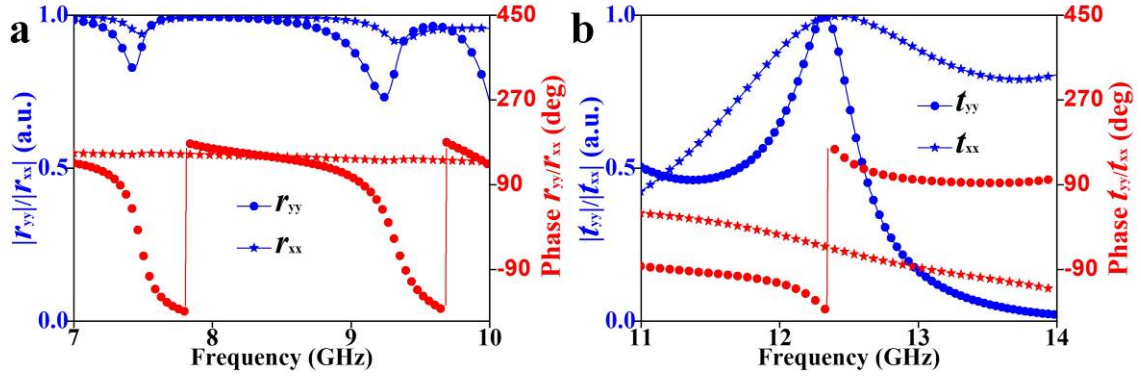


Figure S3 Illustration of the physics for the high efficiency of spin conversion under triple R and T channels.

In the main text, we have shown clear evidence for the individual control at several target frequencies. Here, we afforded comprehensive results in full spectrum to further demonstrate our declaration. Figs. S4~S6 illustrates the effect of individual change of ψ_1 , ψ_2 and ψ_3 for each sub-atom to the total reflection and transmission properties. As is much appreciated from Figs. S4~S6, negligible mode shift and amplitude penalty is observed in all cases when altering ψ_1 , ψ_2 and ψ_3 within $0\sim 150^\circ$ in steps of 30° . Most importantly, individual changing of ψ_1 and ψ_2 only induces elegant reflection and transmission PB phase, respectively without significant phase distortion, indicating a satisfactory suppressed mutual impact. Moreover, the near-unity spin conversion efficiency is inspected in all reflection and transmission modes. Above good feature can also be inspected from the opposite side of the meta-atom (backward channel) in a completely independent manner. Such a proposal finds strong support from Fig. S4, where altering ψ_2 does not pose any influence on the reflection and transmission response of observed side at f_1 , f_2 and f_3 . Such an intriguing isolation is the key for engineering asymmetry forward and backward reflective functions of $F_1\sim F_4$ in both sides.

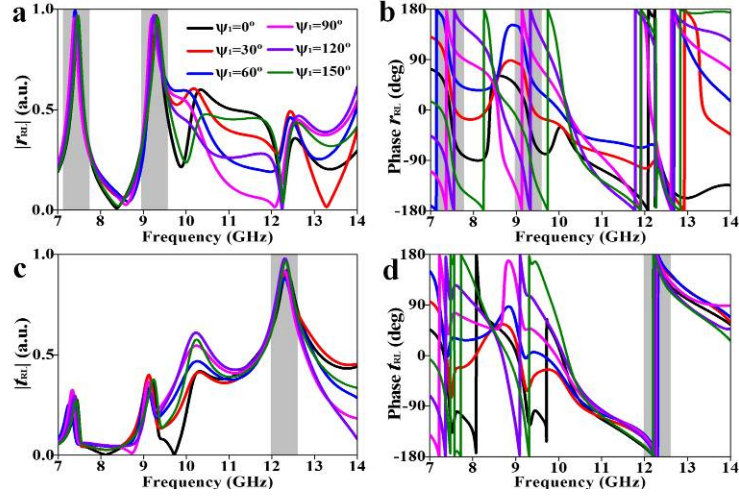


Figure S4 Effect of the rotation ψ_1 to the (a, b) reflection r_{RL} and (c, d) transmission t_{RL} (a, c) amplitude and (b, d) phase properties.

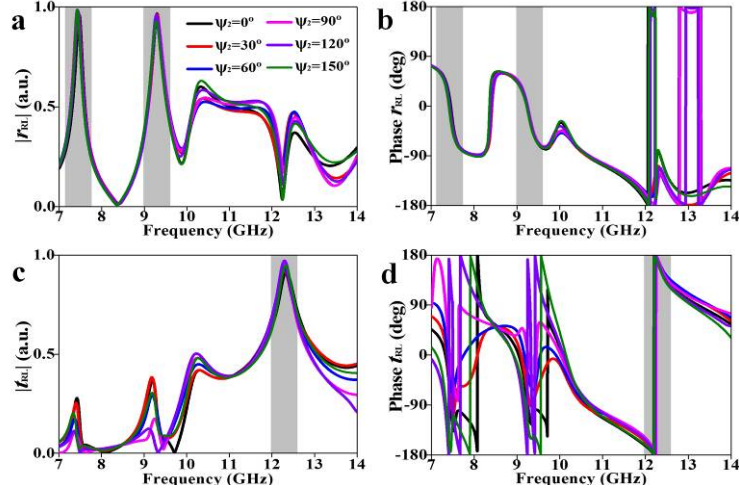


Figure S5 Effect of the rotation ψ_2 to the (a, b) reflection r_{RL} and (c, d) transmission t_{RL} (a, c) amplitude and (b, d) phase properties.

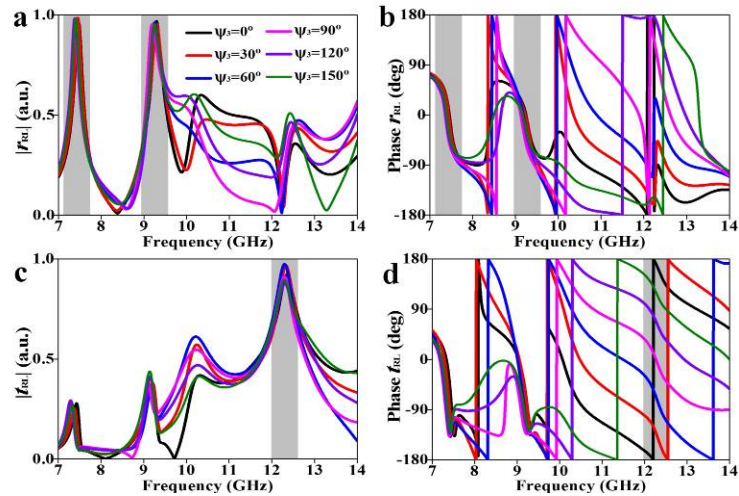


Figure S6 Effect of the rotation ψ_3 to the (a, b) reflection r_{RL} and (c, d) transmission t_{RL} (a, c) amplitude and (b, d) phase properties.

3. Layout of the large-scanning kaleidoscopic-beam generator

Figure S7 portrays the full layout of the top, middle and bottom layer of the full-space kaleidoscopic-beam generator. As can be seen, the ASRR varies spatially along x and y direction in the top and bottom layer, respectively, whereas the evolved H patterns varied synchronously along y direction in both layers. The circular slotted patch in the middle layer are the same at all positions.

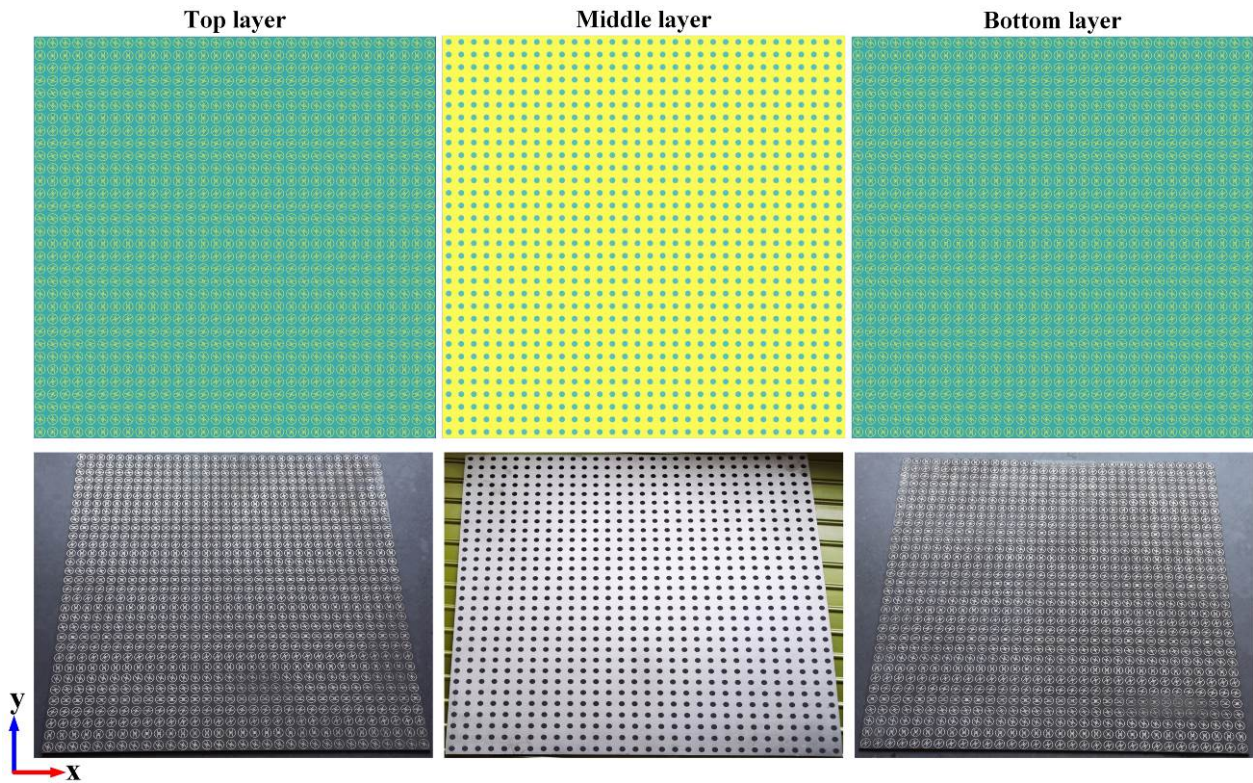


Figure S7 Layout of the triple-layer full-space kaleidoscopic-beam generator based on our chirality-assisted wavelength-space multitasking concept. The top row is the CAD model while the bottom row is the photograph of fabricated sample.

4. Angle-insensitive performance for wide-angle large-capacity reverser

In the main text and previous section, we learned that our composite meta-atom exhibits desired high efficiency of spin conversion under three well-insulated R and T channels mainly under normal incidence. Here, in addition to Fig. 2e we further verify such angle-immune response can also be preserved in two principal incident planes. Figs. S8 and S9 portray the reflection and transmission coefficients in xz and yz plane across a broadband spectrum. As is expected, the transmissive and

reflective amplitude and phase is maintained constant at three grey regions over a large range of incident angles even when θ_i is up to 60° in both planes, indicating a large-angle EM behavior.

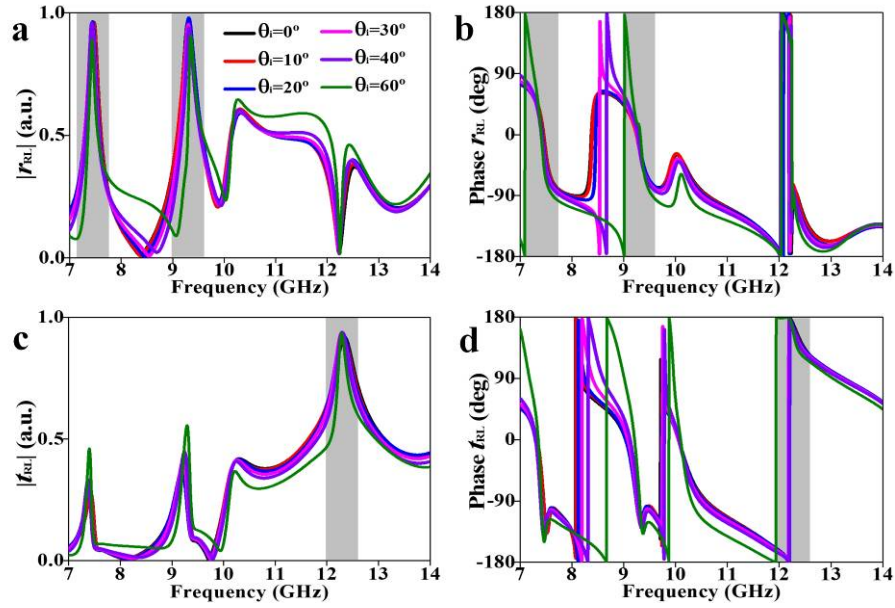


Figure S8 illustration of the angle-immune EM response of the meta-atom at large θ_i when EM wave is incident along xz plane. The total reflection r_{RL} (a, b) and transmission t_{RL} (c, d) amplitude (a, c) and phase (b, d) properties.

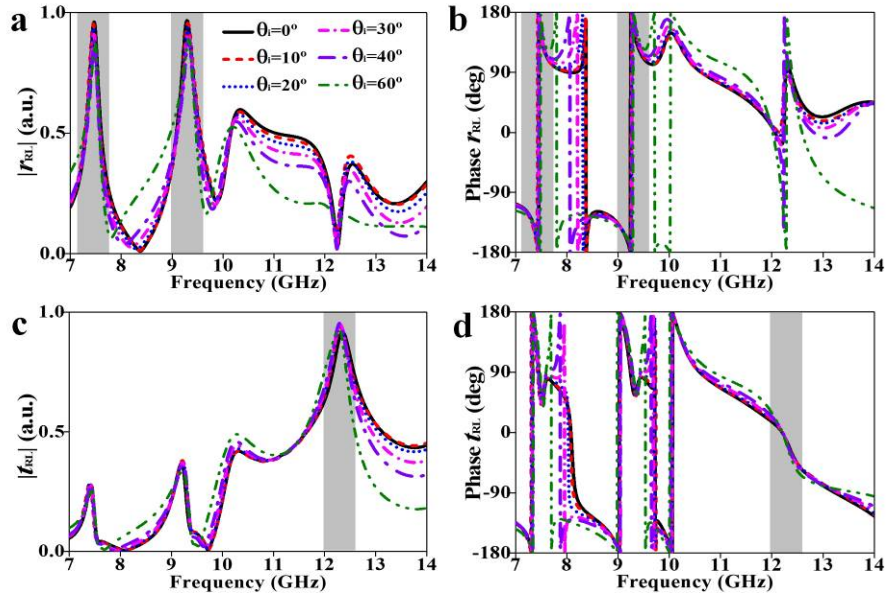


Figure S9 illustration of the angle-immune EM response of the meta-atom at large θ_i when EM wave is incident along yz plane. The total reflection r_{RL} (a, b) and transmission t_{RL} (c, d) amplitude (a, c) and phase (b, d) properties.

In fact, the symmetry-breaking in ASRR is found to account for the angle-immune EM property.

As a proof, we additionally afford the FDTD calculated scattering spectrum for the meta-atom loaded with partial-symmetry SRR under oblique incidence for sharp contrast. The angle-sensitive EM response can be inspected from Fig. S10. As is shown in Figs. S10a and S10b, we only observe one reflection peak around 8.2 GHz when $\theta_i=0^\circ$ and there appears a sharp reflection dip when the EM wave is obliquely incident. Such an amplitude dip is also accompanied with a sharp phase fluctuation across the phase spectrum, indicating an angle-sensitive EM behavior of the partial-symmetry meta-atom. The effect of oblique incidence ($\theta_i=20^\circ$) to the PB phase near 8.2 GHz can be inspected from Figs. S10c and S10d. As is indicated, it is hardly to achieve a linear PB phase response which is two times of the rotation angle ψ_1 when ψ_1 varies from 0° to 150° in steps of 30° . The sharp phase shift under tilt incidence deteriorates the regular PB phase at normal incidence. The sharply varied intensity of excited electric and magnetic dipole modes among different θ_i for SRR meta-atom without symmetry-breaking gives rise to the giant contrast of EM response under large-angle incidence.

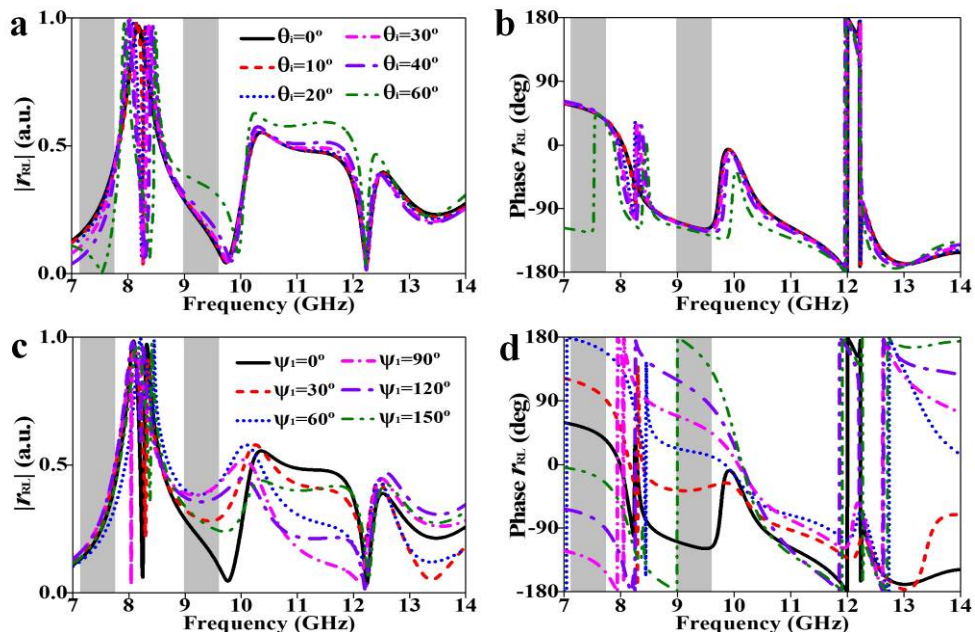


Figure S10 Illustration of the angle-sensitive EM response of the partial-symmetry meta-atom with symmetry split gap. (a) Amplitude and (b) phase response under different incident angles of $\theta_i=0^\circ$,

10°, 20°, 30°, 40°, and 60°, here $\psi_1=\psi_2=\psi_3=0^\circ$. (a) Amplitude and (b) phase response under different ψ_1 of $\psi_1=0^\circ, 30^\circ, 60^\circ, 90^\circ, 120^\circ$, and 150° , here $\theta_1=20^\circ$ and $\psi_2=\psi_3=0^\circ$.

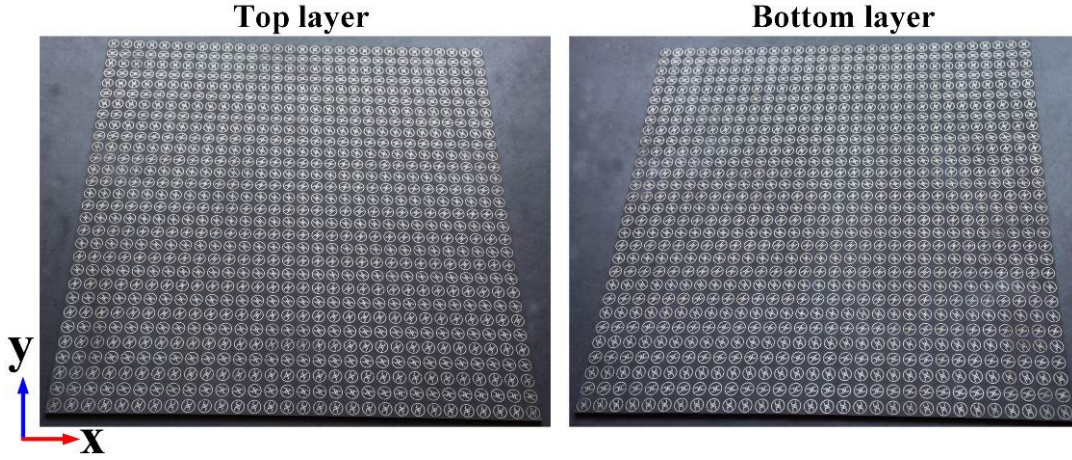


Figure S11 Layout of the triple-layer multitasking full-space retroreflector and negative refractor based on our chirality-assisted wavelength-space multitasking concept. The middle layer is the same with that of fabricated kaleidoscopic-beam generator.

5. Fabrication and experimental setup

The triple-layer metallic patterns of each metadvice are fabricated individually on two dielectric boards using printed-circuit-board (PCB) technique. They were then assembled together through adhesives and finally reinforced through a hot press. In near-field (NF) experiments, the fabricated sample was launched by two types of dual-spin CP horns with voltage-standing-wave ratio (VSWR) less than 2.5 and axial ratio less than 3.5 across 4~8 GHz and 8.2~12.4 GHz, they were fixed with a distance of 0.7 m, see the experimental setup shown in Fig. S12. A 15 mm-long monopole antenna, functioning as the receiver, was placed behind the sample, and connected to an AV3672B vector network analyzer to record the static EM signals. The monopole was fixed to a 2D electronic step motor that can move automatically in a maximum area of 0.7 m×0.7 m with a step resolution of 10 mm. In far-field (FF) experiments, the transmitted horn was placed on one artificially-controlled arm, while the received horn was fixed on the other arm of rotary table which is automatically rotated around the sample in a circumference and controlled by an electronic motor. For

transmission measurement, the sample is enveloped by a mass of radiation-absorbing materials to avoid possible diffractions from the edge of the sample. Under this circumstance, the signal emitted from the horn transmits only through the aperture window while the residual diffractive energy is almost completely blocked.

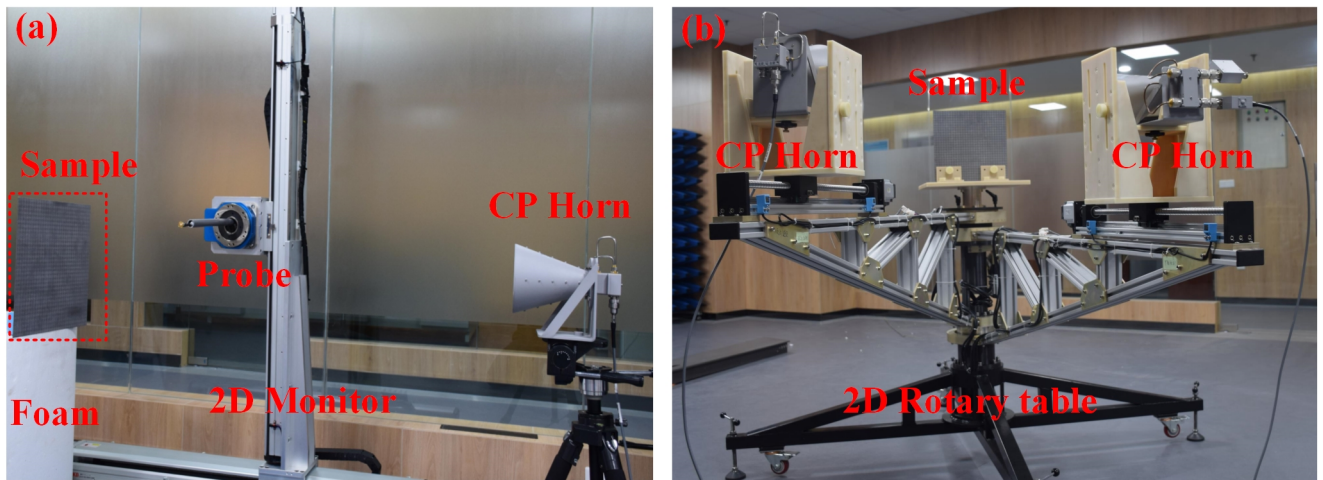


Figure S12 Illustration of the experimental setup for (a) NF and (b) FF measurements.

Figures

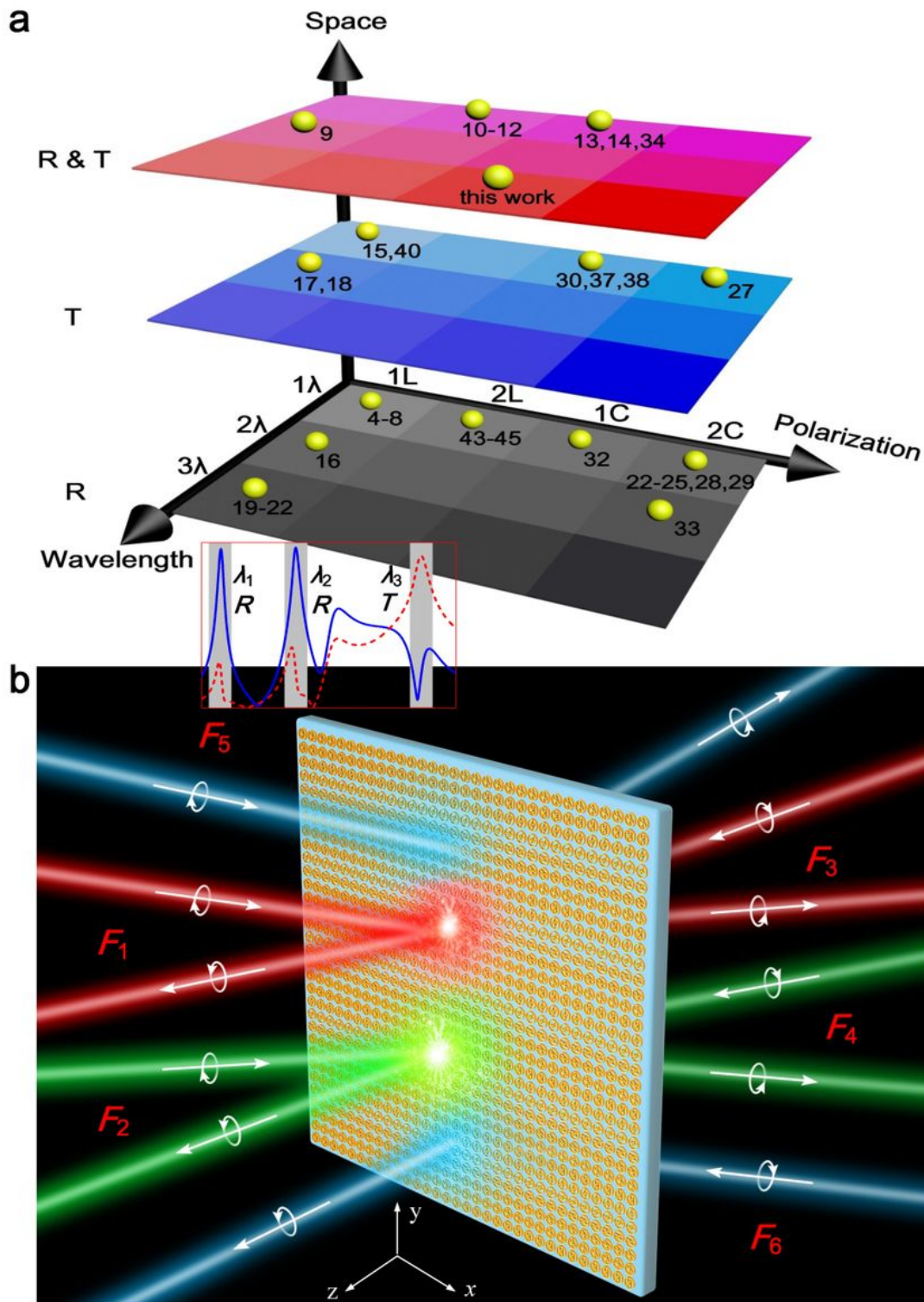


Figure 1

Illustration of the (a) evolution and (b) advanced function of our wavelength-space multitasking Janus metasurface concept for kaleidoscopic full-space spin-wave control. To clearly show the evolutionary process of proposed concept, we summarize existing metasurfaces for EM wave manipulation in a three-

dimensional coordinate system indicated by three information axes of space, wavelength and polarization. Here, the yellow sphere indicating available work with reference numbers marked besides and the gradient panel from light to dark represents the degree of difficulty in realization. The L and C indicate linear and circular polarization (CP), 2L and 2C mean two orthogonal LP and CP wave operations, and R and T indicate reflection and transmission, respectively. Note that the high-efficiency CP operation indicated here requires specific condition of dynamic phases of two orthogonal LP components under LP wave excitations and thus is more difficult than dual-LP operation. Three colours in schematic function represent three synthesized spectrum channels at different operation wavelengths of λ_1 , λ_2 and λ_3 while different angles of each outgoing wave indicate full-space DOA or integrated large-capacity functionalities.

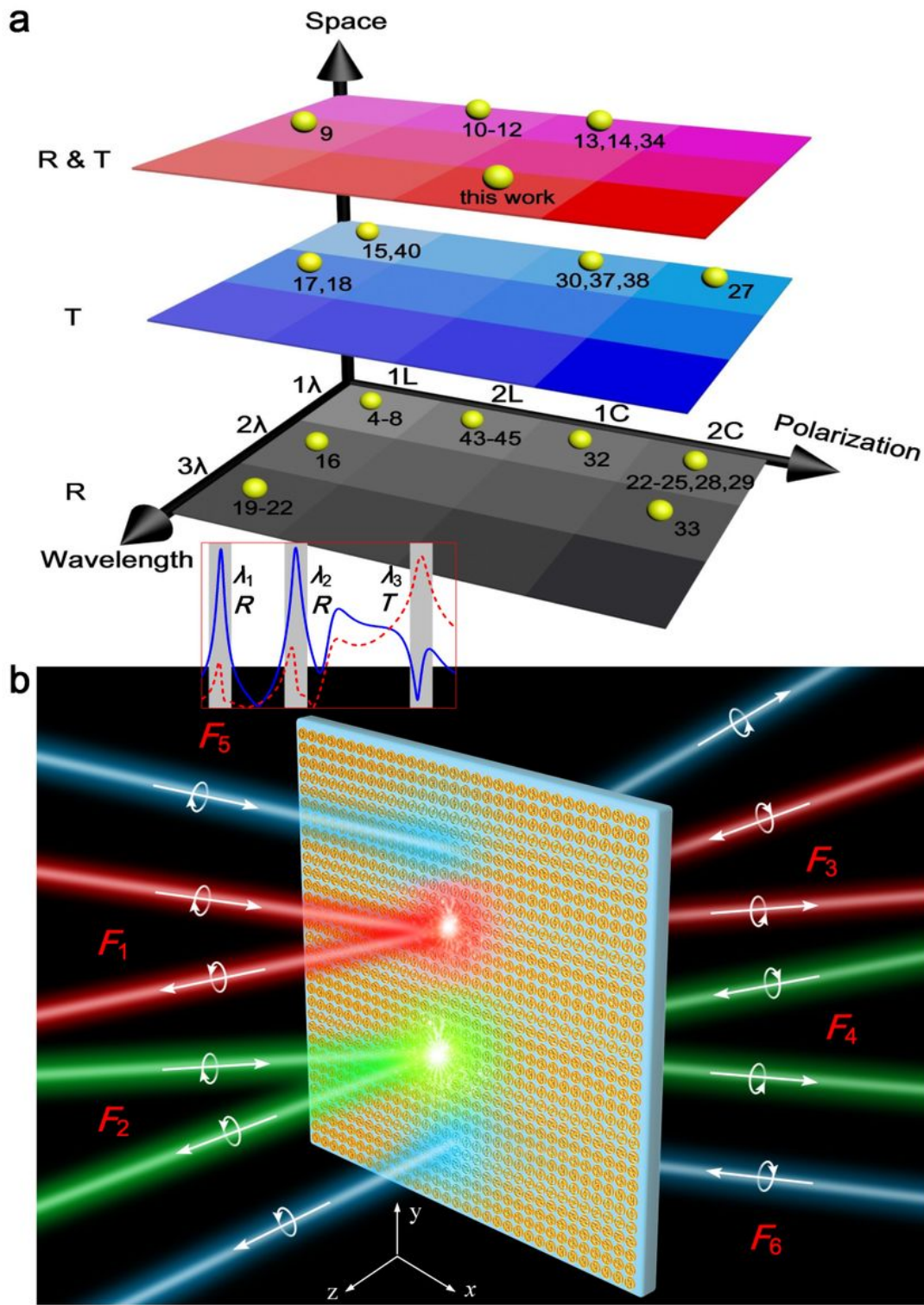


Figure 1

Illustration of the (a) evolution and (b) advanced function of our wavelength-space multitasking Janus metasurface concept for kaleidoscopic full-space spin-wave control. To clearly show the evolutionary process of proposed concept, we summarize existing metasurfaces for EM wave manipulation in a three-dimensional coordinate system indicated by three information axes of space, wavelength and polarization. Here, the yellow sphere indicating available work with reference numbers marked besides

and the gradient panel from light to dark represents the degree of difficulty in realization. The L and C indicate linear and circular polarization (CP), 2L and 2C mean two orthogonal LP and CP wave operations, and R and T indicate reflection and transmission, respectively. Note that the high-efficiency CP operation indicated here requires specific condition of dynamic phases of two orthogonal LP components under LP wave excitations and thus is more difficult than dual-LP operation. Three colours in schematic function represent three synthesized spectrum channels at different operation wavelengths of λ_1 , λ_2 and λ_3 while different angles of each outgoing wave indicate full-space DOA or integrated large-capacity functionalities.

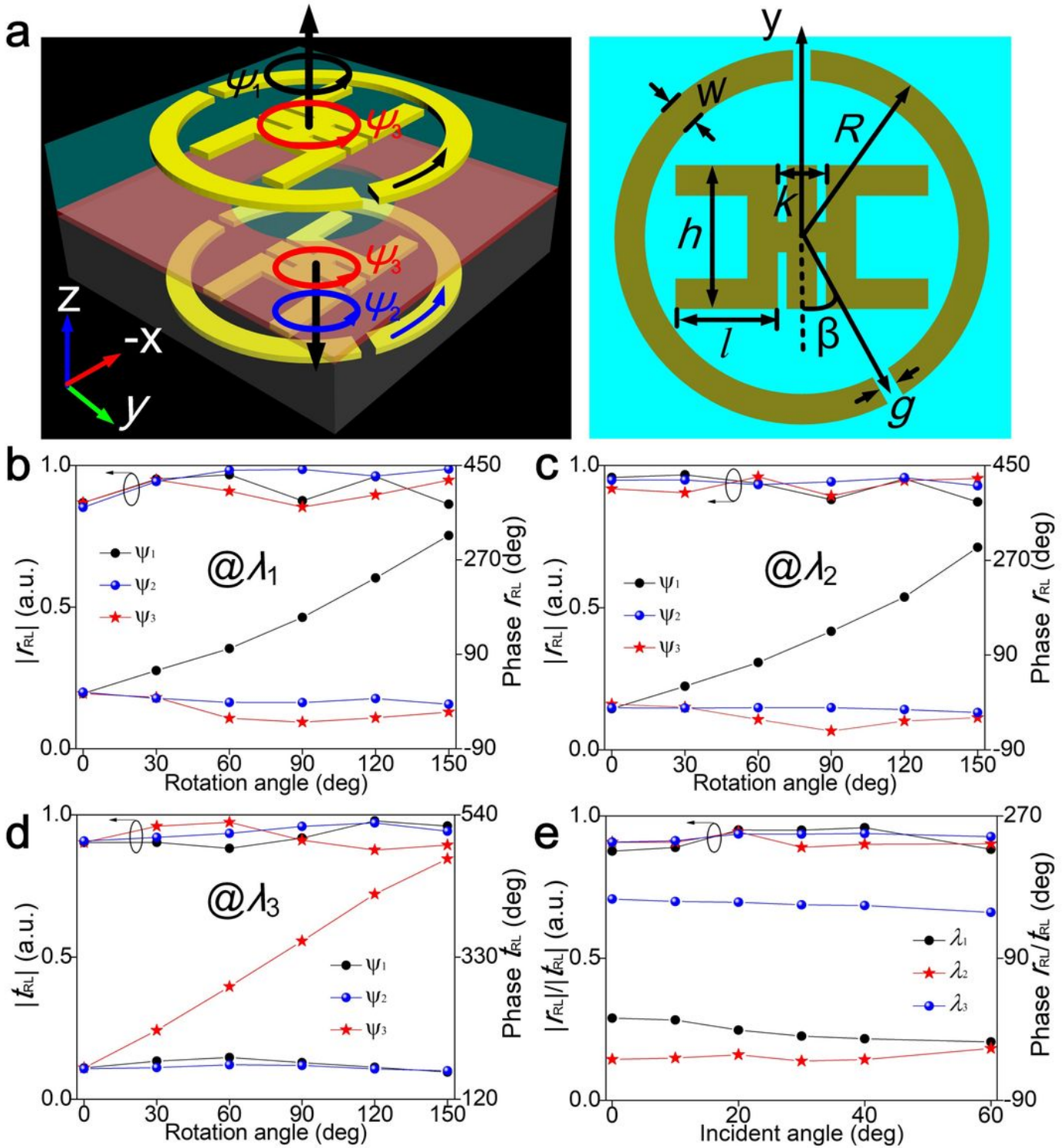


Figure 2

Characterization of the composite meta-atom for wavelength-space multitasking when the EM wave illuminates from the forward side. Similar results and conclusion can be drawn in backward case. Here, both dynamic and geometric phases are utilized to construct the predesigned functions with high efficiency by rotating each of well-designed sub-atoms along its central axis, for example the orientation of the top and bottom ASRR (ψ_1 and ψ_2) and the entire dual-layer evolved H (ψ_3). (a) Layout and

parametric illustration, here, detailed structure parameters are $p_x=p_y=10$, $k=1.4$, $h=3$, $l=2.2$, $w=0.4$, $g=0.4$, $R=4.15$ mm, $\beta=20^\circ$ and the radius of circular slot in middle layer is 2.3 mm. The commonly available F4B board with a dielectric constant $\epsilon_r=2.65$, loss tangent $\tan\delta=0.001$, and thickness $h=1$ mm is utilized as the dielectric spacer. Effects of ψ_1 , ψ_2 and ψ_3 to the spin-conversion reflection r_{RL} at (b) λ_1 , (c) λ_2 and to the spin-conversion transmission t_{RL} at (d) λ_3 . (e) The angle-immune EM response (r_{RL} at λ_1 , λ_2 and t_{RL} at λ_3) of the composite meta-atom as a function of . Here, the left and right scale is plotted for amplitude and phase, respectively.

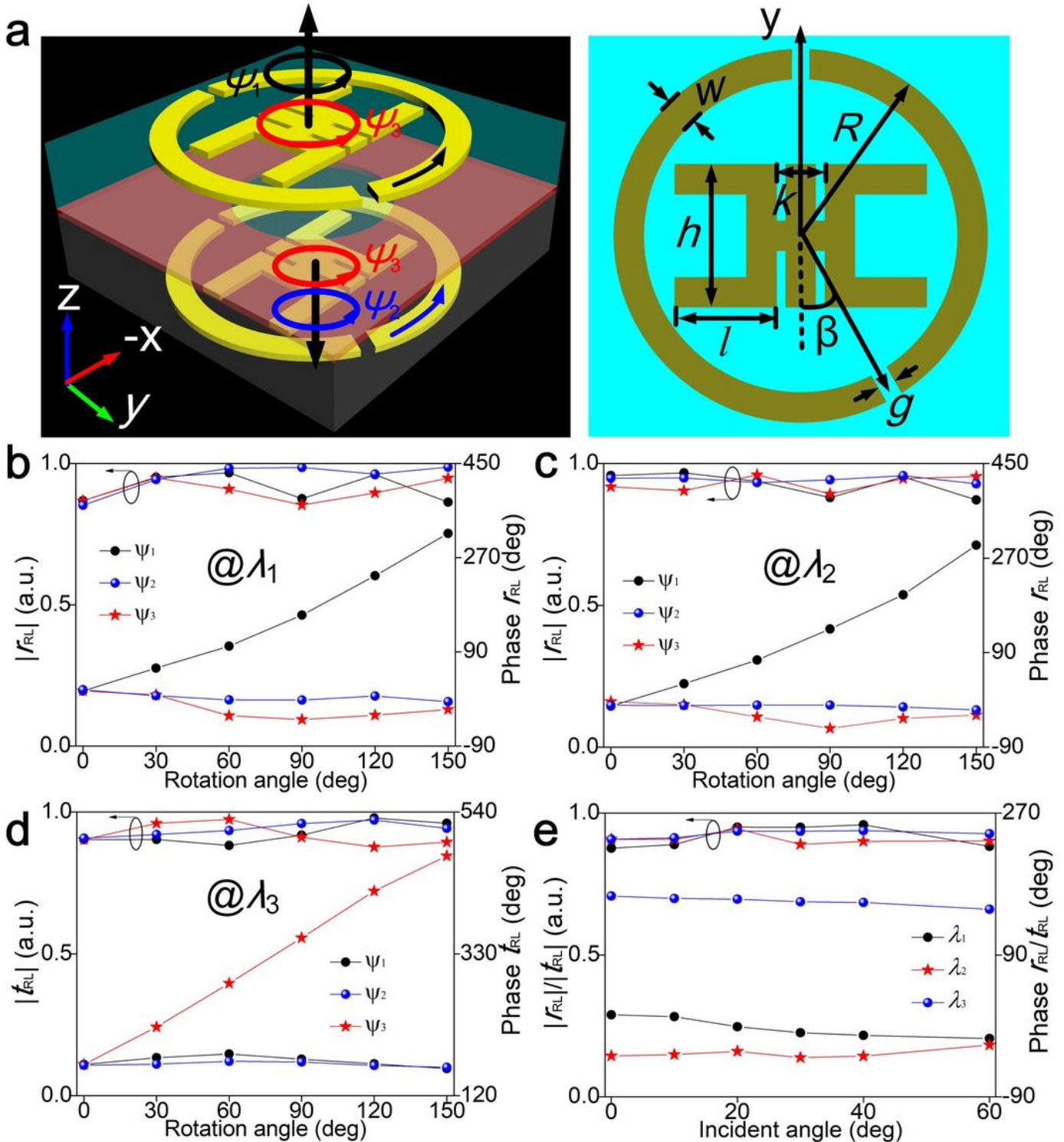
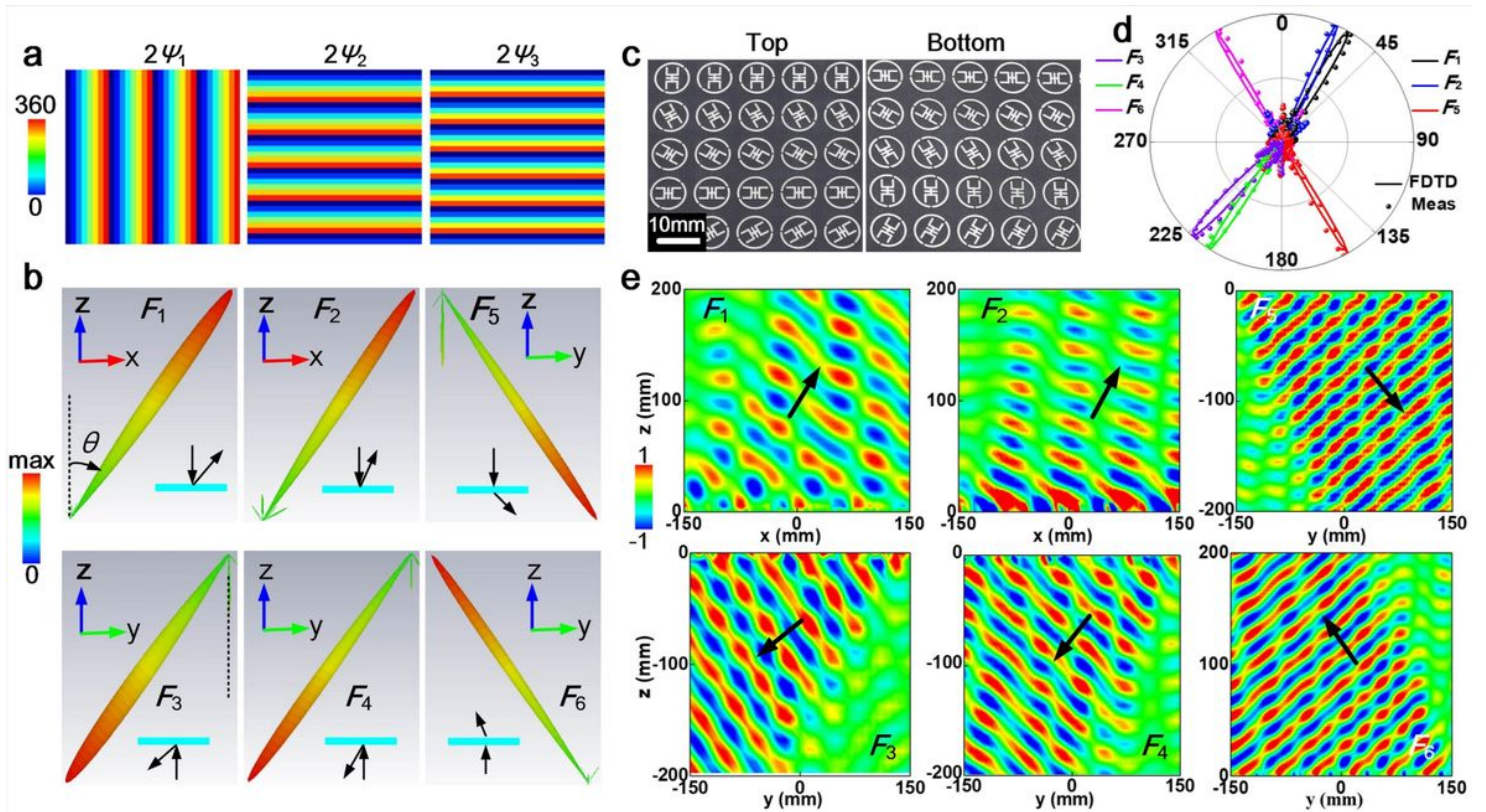


Figure 2

Characterization of the composite meta-atom for wavelength-space multitasking when the EM wave illuminates from the forward side. Similar results and conclusion can be drawn in backward case. Here, both dynamic and geometric phases are utilized to construct the predesigned functions with high efficiency by rotating each of well-designed sub-atoms along its central axis, for example the orientation of the top and bottom ASRR (ψ_1 and ψ_2) and the entire dual-layer evolved H (ψ_3). (a) Layout and parametric illustration, here, detailed structure parameters are $p_x=p_y=10$, $k=1.4$, $h=3$, $l=2.2$, $w=0.4$, $g=0.4$, $R=4.15$ mm, $\beta=20^\circ$ and the radius of circular slot in middle layer is 2.3 mm. The commonly available F4B board with a dielectric constant $\epsilon_r=2.65$, loss tangent $\tan\delta=0.001$, and thickness $h=1$ mm is utilized as the dielectric spacer. Effects of ψ_1 , ψ_2 and ψ_3 to the spin-conversion reflection rRL at (b) λ_1 , (c) λ_2 and to the spin-conversion transmission tRL at (d) λ_3 . (e) The angle-immune EM response (rRL at λ_1 , λ_2 and tRL at λ_3) of the composite meta-atom as a function of θ . Here, the left and right scale is plotted for amplitude and phase, respectively.

**Figure 3**

Characterization of the multitasking kaleidoscopic-beam generator for full-space DOA comprising 32×32 meta-atoms and occupying an area of 320×320 mm². (a) Required phase distributions in 2D profile (top panel) and along centre line (bottom panel). Three types of phase gradients $\xi=2\pi/np$ imposed along x and y directions of each forward or backward channel with n the number of meta-atoms in a supercell (here n is 8, 6 and 5 for ξ_1 , ξ_2 and ξ_3 , respectively). (b) FDTD calculated FF scattering patterns for functions of $F_1 \sim F_6$. (c) Zoom-in view of the fabricated sample. (d) Comparison of FF scattering cross-

section intensity between FDTD calculations and experiments. (e) Experimentally measured NF patterns (E field) in xz and yz planes.

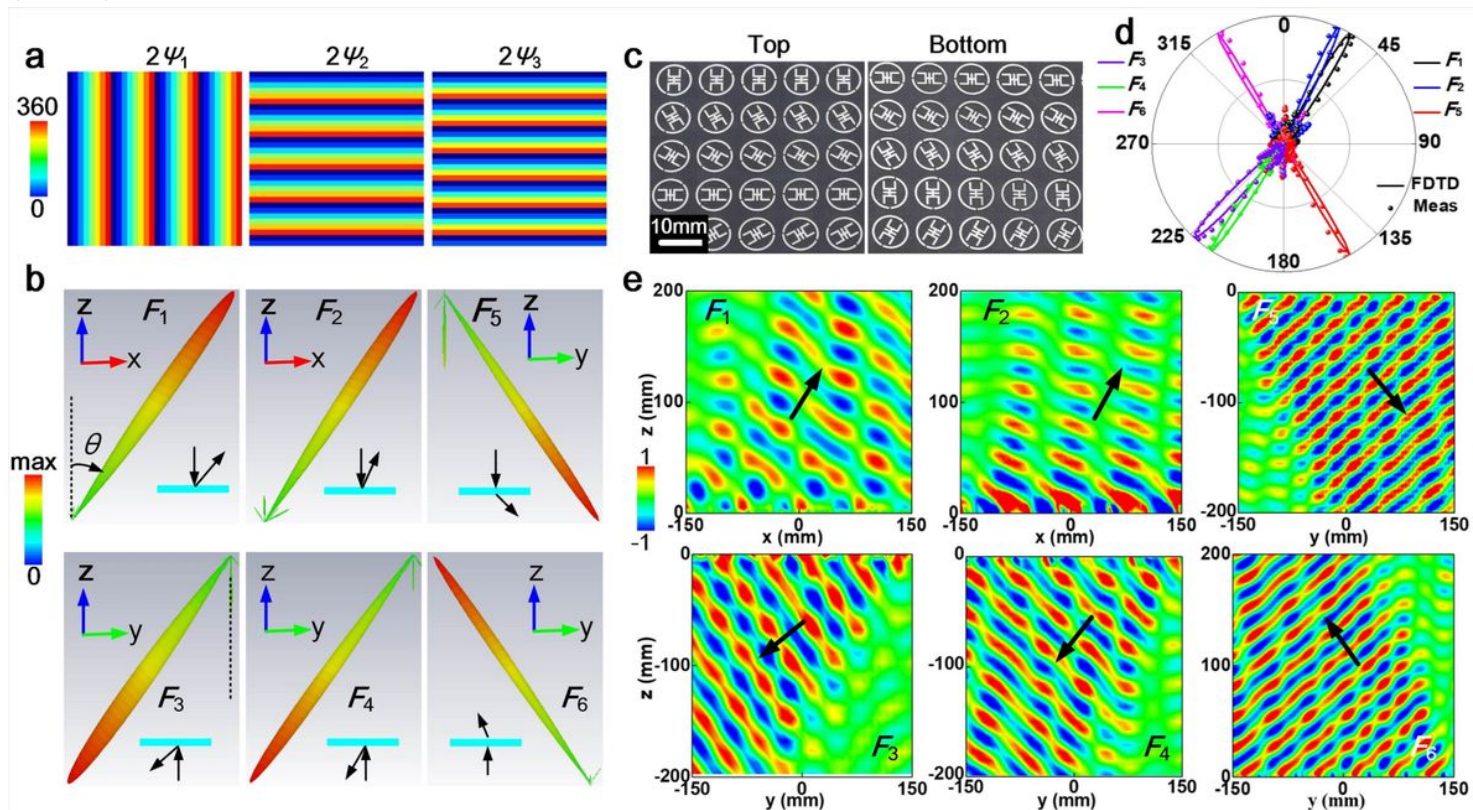


Figure 3

Characterization of the multitasking kaleidoscopic-beam generator for full-space DOA comprising 32×32 meta-atoms and occupying an area of 320×320 mm². (a) Required phase distributions in 2D profile (top panel) and along centre line (bottom panel). Three types of phase gradients $\xi = 2\pi/np$ imposed along x and y directions of each forward or backward channel with n the number of meta-atoms in a supercell (here n is 8, 6 and 5 for ξ_1 , ξ_2 and ξ_3 , respectively). (b) FDTD calculated FF scattering patterns for functions of $F_1 \sim F_6$. (c) Zoom-in view of the fabricated sample. (d) Comparison of FF scattering cross-section intensity between FDTD calculations and experiments. (e) Experimentally measured NF patterns (E field) in xz and yz planes.

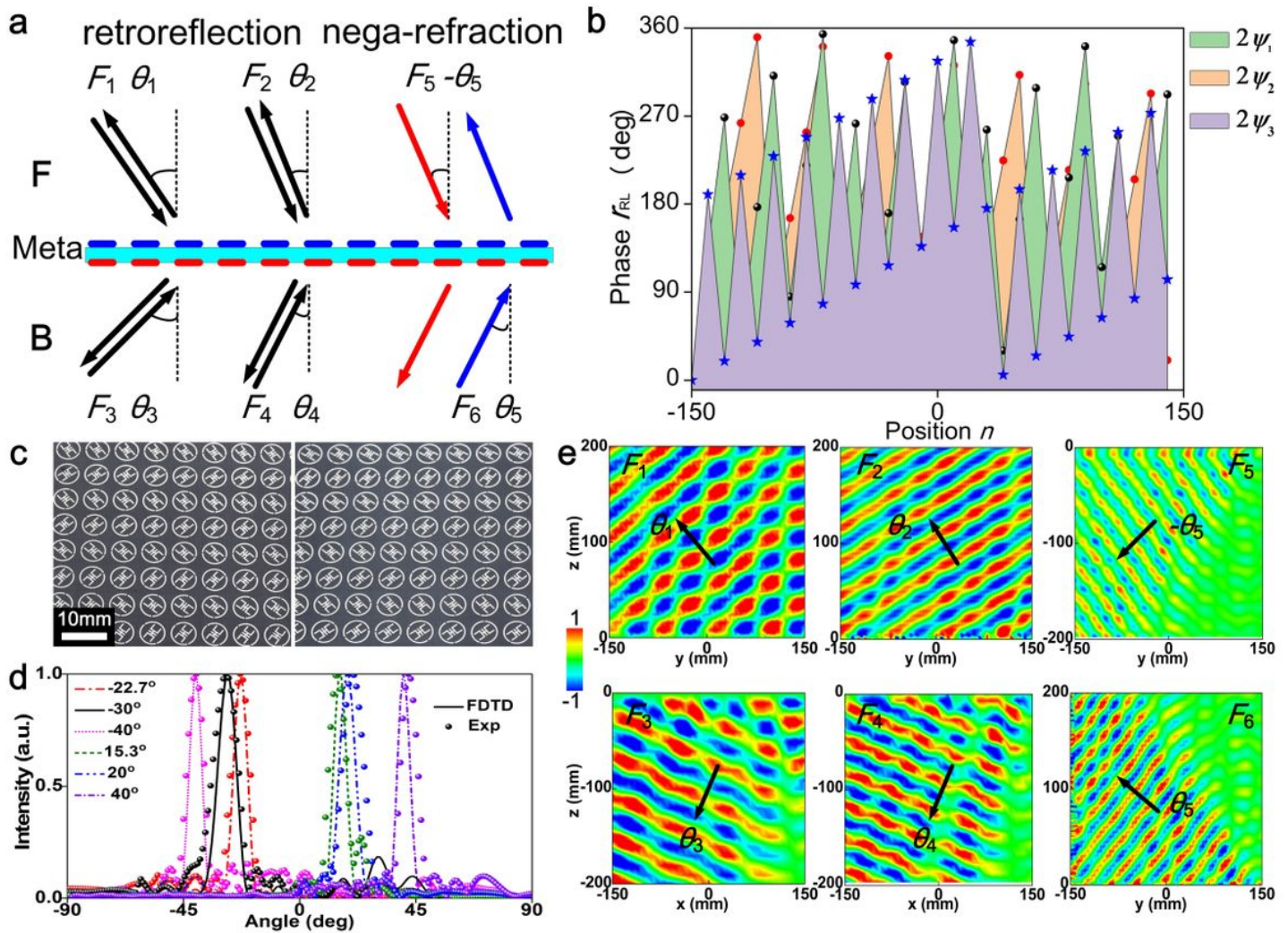


Figure 4

Characterization of the multitasking reverser (integrated retroreflector and negative refractor) for full-space DOA comprising 30×30 meta-atoms and occupying an area of $300 \times 300 \text{ mm}^2$. (a) Illustration of the schematic functionality. (b) Required phase distributions in 2D profile (top panel) and along centre line (bottom panel). (c) Zoom-in view of the fabricated sample. (d) Comparison of FF scattering cross-section intensity between FDTD calculations and experiments. (e) Experimentally measured NF patterns (E field) in xz and yz planes for functions of $F_1 \sim F_6$. Here, the reflection or refraction angle is defined with respect to the normal within $-90^\circ \sim 90^\circ$ and all measured results intensity are normalized against its maximum.

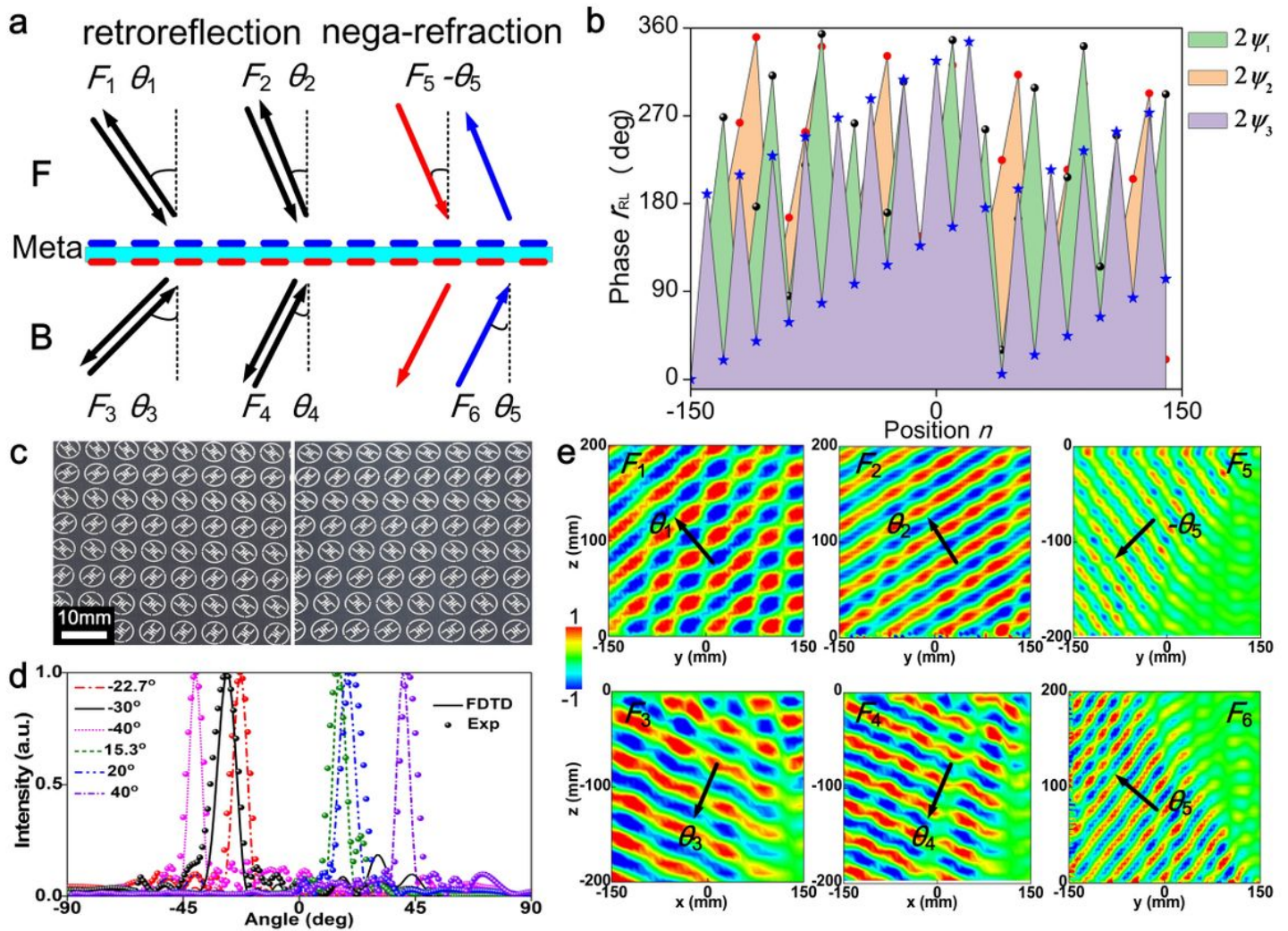


Figure 4

Characterization of the multitasking reverser (integrated retroreflector and negative refractor) for full-space DOA comprising 30×30 meta-atoms and occupying an area of 300×300 mm². (a) Illustration of the schematic functionality. (b) Required phase distributions in 2D profile (top panel) and along centre line (bottom panel). (c) Zoom-in view of the fabricated sample. (d) Comparison of FF scattering cross-section intensity between FDTD calculations and experiments. (e) Experimentally measured NF patterns (E field) in xz and yz planes for functions of $F_1 \sim F_6$. Here, the reflection or refraction angle is defined with respect to the normal within $-90^\circ \sim 90^\circ$ and all measured results intensity are normalized against its maximum.

Supplementary Files

This is a list of supplementary files associated with this preprint. Click to download.

- [FigS1.jpg](#)

- FigS1.jpg
- FigS2.jpg
- FigS2.jpg
- FigS3.jpg
- FigS3.jpg
- FigS4.jpg
- FigS4.jpg
- FigS5.jpg
- FigS5.jpg
- FigS6.jpg
- FigS6.jpg
- FigS7.jpg
- FigS7.jpg
- FigS8.jpg
- FigS8.jpg
- FigS9.jpg
- FigS9.jpg
- FigS10.jpg
- FigS10.jpg
- FigS11.jpg
- FigS11.jpg
- FigS12.jpg
- FigS12.jpg